EXPERIMENTAL TECHNIQUES TO STUDY THE EFFECTS OF NANOPARTICLE ADDITIVES ON HETEROGENEOUS MONOPROPELLANT COMBUSTION

A Thesis

by

KENNETH WOODROW MCCOWN III

Submitted to the Office of Graduate and Professional Studies of
Texas A&M University
in partial fulfillment of the requirements for the degree of

MASTER OF SCIENCE

Chair of Committee,	Eric Petersen
Committee Members,	Andrea Strzelec
	Adonios Karpetis
Head of Department,	Andreas Polycarpou

May 2014

Major Subject: Mechanical Engineering

ABSTRACT

This thesis presents the development of techniques used to investigate the combustion behavior of liquid monopropellants with or without additives, with a focus on nano-scale particles as burning rate modifiers in nitromethane. The linear burning rates of these mixtures were measured in a constant-volume system at chamber pressures ranging from 3 to 14 MPa, all without direct observation of the propellant burning front. Distinct differences in burning rates were observed between burns using a quartz-lined cavity and those employing plain carbon steel. Several analytical models and numerical approximations were used to estimate the temperature profiles of quartz, steel, and layered strand burner tubes, indicating that the higher burning rates measured in the steel cavity were likely caused by a combination of heat transfer and catalytic effects. The close match between the burning rates of neat nitromethane gathered in this study and those taken from recent studies utilizing optical systems proves the utility of the author's method, while the consistently measured burning rates of the various nitromethane-based nanofluids prove the versatility of the same method when extended to tests on suspended-particle mixtures

Nano-scale aluminum was used to increase the overall energy density of propellant mixtures, fumed silica powder was used to increase the mixture thickness and encourage aluminum suspension, and nano-scale titania was also included based on its previous use as a burning rate modifier in solid propellants. The silica loading was varied from 1% to 3% by weight, aluminum loading was varied from 5% to 13.5% by

weight, and titania was added at 1% by weight. A comprehensive settling study was used to characterize the stability of numerous propellant mixtures, quantifying the particle settling rates of unstable mixtures while subsequently eliminating this instability from all burned configurations. This thesis observed a wide variety of particle effects on the combustion behavior of nitromethane; some of these trends were previously observed by other research groups, while several burning rate effects were observed by the current author for the first time. These novel behavioral trends included an increase in propellant pressure sensitivity over the tested 3- to 14-MPa range for mixtures that included 3% silica by weight, and an even more dramatic increase in pressure sensitivity and linear burning rates was observed only at chamber pressures above 8 MPa for propellants that included 1% titania by weight without silica. The various performance trends uncovered and techniques developed through this study have already been applied to new mixtures based on more exotic compounds, utilizing the lessons learned herein as a springboard to greatly expand the range of propellants currently tested at Texas A&M University.

ACKNOWLEDGMENTS

I would like to thank my research advisor and thesis committee chair, Dr. Eric Petersen, for his continuous guidance and support during my time as an undergraduate and graduate researcher at Texas A&M University. The time I have spent working in his lab has been an immensely rewarding experience, and the lessons I have learned will continue to shape my development as an engineer long after I have graduated. I would also like to thank the additional members of my thesis committee, Dr. Andrea Strzelec and Dr. Adonios Karpetis, for their dedication and instruction during the course of my graduate studies.

Thanks go to my friends and fellow researchers in the Petersen Rocket Propellant Group for fostering an environment of openness and collaboration: Andrew Demko, Chris Thomas, Tyler Allen, Tom Sammet, and Will Warren. I would also like to acknowledge Dr. Stanislav Vitha from the Microscopy and Imaging Center at Texas A&M University for his efforts in providing microscopic images of the nanoparticle additives.

Finally, I would like to thank my family for always providing an encouraging word, often dispensing helpful advice, and never hesitating to answer the occasional midnight phone call. Their efforts and the core values they instilled in me have made me who I am today.

NOMENCLATURE

Linear Burning Rates

a	Burning rate empirical coefficient
d	Burner tube cavity diameter
m	Burned propellant mass
n	Burning rate pressure exponent
P	Chamber pressure
r_b	Linear burning rate
T_p	Initial propellant temperature
Y_i	Individual propellant component mass fraction
Δr_b	Change in linear burning rate
Δt	Total burning time
Δx	Burned propellant axial length
ρ	Overall propellant mixture density
ρ_i	Individual propellant component density

Heat Transfer Models

F	Temperature profile initial function
h	Ambient fluid convection coefficient
H	Modified convection coefficient
J_ν	Bessel function of the first kind of order ν

k_i	Burner tube thermal conductivity
L	Burner tube length
N	Temperature profile norm
q'	Heat transfer rate per unit length
r	Radial position
r_i	Radius at burner tube material boundary
R_0	Radial temperature profile eigenfunction
t	Time
T	Temperature
T_i	Temperature at burner tube material boundary
T_s	Propellant burning surface temperature
$T_{r,t}$	Finite-difference temperature at radius r and time t
$T_{x,t}$	Finite-difference temperature at height x and time t
T_0	Initial burner tube temperature
T_∞	Ambient fluid temperature
x	Axial position
X	Axial temperature profile eigenfunction
Y_ν	Bessel function of the second kind of order ν
α	Burner tube thermal diffusivity
β_i	Temperature profile eigenvalue
δr	Finite-difference radius step
δt	Finite-difference time step

δx	Finite-difference height step

Common Acronyms

AP	Ammonium perchlorate
EIL	Energetic ionic liquid
HAN	Hydroxylammonium nitrate
HTPB	Hydroxyl-terminated polybutadiene
LFB	Liquid-fed burner
ProPEP	Propellant Performance Evaluation Program
QTH	Quartz-tungsten-halogen
STB	Static tube burner
TEM	Transmission electron microscopy

TABLE OF CONTENTS

Page

LIST OF FIGURES

Page

LIST OF TABLES

1. INTRODUCTION*

1.1. Motivation for Current Study

For many years, hydrazine has been utilized as the primary monopropellant in a wide variety of aerospace applications, ranging from the first stage of the Titan II to the cruise stage of the recently launched Mars Science Laboratory. Within the last two decades, the severe health and environmental risks posed by toxic hydrazine (N_2H_4) and hydrazine-based compounds have renewed interest in the development of alternative monopropellants. In the wake of this search, energetic ionic liquids (EILs), peroxides, and other monopropellants have emerged as possible replacements for hydrazine [1-3]. The low vapor pressures, reduced toxicities, and high thermal stabilities of most of these alternative propellants address many of the handling and storage concerns posed by hydrazine-based materials [4].

One propellant in particular—nitromethane (CH_3NO_2)—is already used in numerous industrial applications that include fuel additives and explosives, and it possesses a higher energy density and higher specific impulse than current hydrazine-based monopropellants [5]. These useful physical properties, combined with a low material cost and widespread production, make nitromethane an ideal candidate for controlled evaluation in a laboratory environment. The results of such a study could be

---

*Part of this section is reprinted with permission from:
K.W. McCown III, A.R. Demko, E.L. Petersen, J. Propul. Power (2014) in press,
DOI: 10.2514/1.B35093, Copyright 2013 by the American Institute of Aeronautics and Astronautics;
K.W. McCown III, E.L. Petersen, Combust. Flame (2014) in press,
DOI: 10.1016/j.combustflame.2013.12.019, Copyright 2013 by the Combustion Institute.

used to aid the development of nitromethane as a viable monopropellant in its own right and guide the testing and development of other hydrazine alternatives.

Like nitromethane, EILs based on aqueous solutions of hydroxylammonium nitrate (HAN) have also been shown to possess improved performance characteristics when compared to hydrazine [6]. These propellants typically consist of three major components: HAN, water, and a compatible reducing agent such as triethanol ammonium nitrate, glycine, or methanol [7-10]. However, the expense and difficulty in obtaining concentrated solutions of HAN and the added complexity of the three-part baseline mixtures make these propellants less desirable for use during the development of entirely new experimental methods. In such cases, the use of nitromethane could provide a simplified means of evaluating untried testing procedures and equipment without exhausting a laboratory's supply of rarer EILs.

The performance of nitromethane and other monopropellants can be enhanced through the addition of metal and metal oxide additives, increasing their energy densities and specific impulses. This ability to tailor combustion behavior greatly increases the range of useful scenarios for these alternative propellants, further promoting their use as viable replacements for hydrazine. Advancements in the manufacture of nanoparticles have yielded a wide array of recent studies involving the combination of nano-scale particles and liquid propellants to create combustible nanofluids [3,11,12]. The relative stability and safety of nitromethane allow researchers to concentrate solely on the tailoring of combustion behavior through this nanoparticle addition, uncovering

performance trends that will guide future additive studies completed with more exotic monopropellants, such as EILs.

1.2. Overview of Thesis

This thesis focuses on the development of techniques to measure the linear burning rates of both liquid monopropellants and heterogeneous mixtures and their subsequent use to explore the effects of added nano-scale particles on propellant combustion. Nitromethane was chosen as the basis for all tested propellants due to its aforementioned stability and ease of access, while various concentrations of aluminum, fumed silica, and titania nanoparticles were used to alter burning behavior.

After providing a background on relevant nitromethane combustion studies, the experimental techniques used to evaluate the burning behavior of various nitromethane-based nanofluids are described. Additional measures taken to quantify particle settling and eliminate it from tested propellant configurations are also included. The nitromethane burning rates gathered with this method are then compared to those measured by previous groups, validating the authors' process. To explain variations in the performance of tested nitromethane between burner configurations that utilized different cavity materials, several analytical models and numerical approximations of the burner tube temperature profile are illustrated and compared. By also evaluating the consistency of burning rate measurements taken for neat nitromethane and mixtures containing suspended silica and aluminum particles, the method's viability for testing both homogeneous and heterogeneous propellants is proven. The separate and combined

effects of the nanoparticle additives were compared to isolate the influence of each material on the empirical coefficient and pressure exponent of the burning rate equation for the resulting nanofluid propellant.

In contrast to the limitations imposed by direct observation methods, the technique described herein greatly expands the range of useful burner configurations and materials and obviates the need for costly observation equipment. The effects of a wide variety of particle additives and respective weight concentrations in included within the current thesis, confirming several previous observations made by other research groups and uncovering additional trends that encourage further study.

2. BACKGROUND*

2.1. Nitromethane

Nitromethane is a clear, colorless liquid at room temperature with a viscosity of 0.61 mPa-s and atmospheric freezing and boiling points of -28.6 and 101.2 °C, respectively. As previously mentioned, the elevated energy density and superior handling properties of nitromethane make it an excellent candidate for future monopropellant applications and use as a surrogate for the development of other alternatives to hydrazine-based fuels. The major physical and performance characteristics of nitromethane are compared to currently used hydrazine in Table 1. Densities were taken for materials at a typical laboratory temperature of 20 °C, while the performance characteristics were calculated using the Propellant Performance Evaluation Program (ProPEP 3) for a 50:1 nozzle exhausted from a 1000-psia combustion chamber into a vacuum.

A higher LD_{50} toxicity rating indicates that a larger dose is required for lethal effect, making nitromethane significantly less toxic than hydrazine. Short-term exposure to small quantities of hydrazine has been shown to result in seizures, comas, and significant damage to the central nervous system in humans, while long-term exposure has been shown to result in severely carcinogenic growths in tested animals. In contrast,

---

*Part of this section is reprinted with permission from:
K.W. McCown III, A.R. Demko, E.L. Petersen, J. Propul. Power (2014) in press,
DOI: 10.2514/1.B35093, Copyright 2013 by the American Institute of Aeronautics and Astronautics;
K.W. McCown III, E.L. Petersen, Combust. Flame (2014) in press,
DOI: 10.1016/j.combustflame.2013.12.019, Copyright 2013 by the Combustion Institute.

nitromethane has been found to be relatively harmless with adequate lab ventilation; respiration and central nervous system effects have been reported at extremely high vapor concentrations, but these effects were typically much less severe than those of relatively dilute hydrazine [5].

Table 1. Selected physical and performance characteristics for nitromethane and hydrazine.

Propellant	Nitromethane	Hydrazine
Molecular Weight (g/mol)	61.04	32.05
Density (g/cm^3)	1.138	1.013
Specific Impulse (s)	289.1	233.8
Density Impulse ($g\text{-}s/cm^3$)	329.0	236.8
Adiabatic Flame Temperature (°C)	2191	1121
LD_{50} Toxicity (mg/kg)	940	60

2.2. Previous Studies

In the years directly after the Second World War, Naval Ordnance conducted a series of tests to measure the burning rate of nitromethane as a function of chamber pressure from 8 to 172 MPa [13]. Similar burning rate studies were conducted two decades later by Raikova in Moscow at pressures ranging from 6.5 to 30 MPa [14]. After a decades-long period of reduced interest, the recent desire to replace toxic hydrazine has brought nitromethane back to the forefront and broadened the variety of monopropellant ignition techniques to include newer resonant lasers [15] along with the older nickel-chromium wire [16,17].

In 1997, Boyer *et al*. from the Pennsylvania State University measured the temperature sensitivity and intrinsic burning rate of nitromethane in a liquid-fed burner (LFB) system [18]. Two years later, Kelzenberg *et al*. studied the burning rate of nitromethane under strand burner conditions and created a simplified model of its combustion behavior [19]. Members of the Pennsylvania State research group continued to study the behavior of nitromethane and employed a static tube burner (STB) in addition to the original LFB system, noting that the system configuration had significant impact on measured linear burning rates [5,20]. These studies produced two disparate burning rate trends at the observed pressures between 3 and 15 MPa; the LFB resulted in consistently faster burning rates than the STB over the tested pressure range.

The extensive range of chamber pressures used to test the burning rate of nitromethane stretches from 0.5 to 172 MPa, and these disparate studies can be combined to reveal the presence of several different pressure regimes of burning behavior [5]. Within each of these pressure regimes, the linear burning rate of nitromethane (r_b) is defined using the same numerical form shown in Eq. (1), but with a unique empirical coefficient that can be used to describe initial temperature dependence (a) and an exponential factor that describes pressure dependence (n)—commonly known as the pressure exponent [21].

$$r_b = aP^n \tag{1}$$

In a dissertation that culminated several studies on nitromethane combustion, Boyer identified the three major regimes of nitromethane burning behavior that acted in

accordance with Eq. (1) [5]. These burning rate equations, along with their respective pressure ranges, are provided in Eqs. (2-4).

$$r_b[mm/s] = 0.173\ (P[MPa])^{1.17} \quad (3 < P \leq 15\ MPa) \tag{2}$$

$$r_b[mm/s] = 0.009\ (P[MPa])^{2.33} \quad (15 < P \leq 70\ MPa) \tag{3}$$

$$r_b[mm/s] = 4.153\ (P[MPa])^{0.86} \quad (70 < P \leq 170\ MPa) \tag{4}$$

The most recent combustion studies on nitromethane and nitromethane-based propellant mixtures focused on the specific pressure regime existing from 3 to 15 MPa; the pressure range of the current study was set at similar values of 3 and 14 MPa to facilitate a direct comparison of results herein to those gathered by previous groups [5,20,22-24]. The disparate ranges of nitromethane burning rates taken from previous studies are compiled in Fig. 1, along with a magnified view of those rates that correspond to the pressure range of interest for the current study.

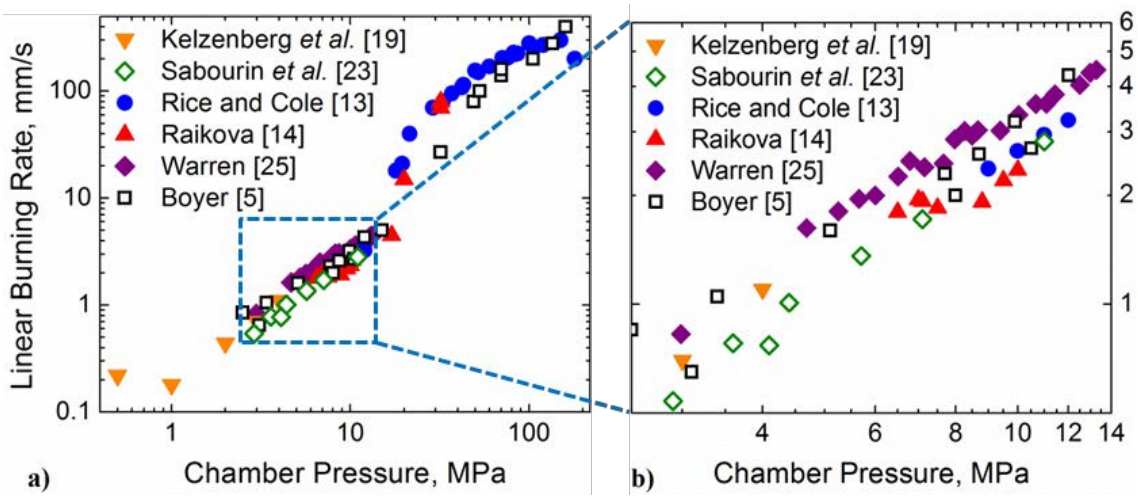

Fig. 1. Burning rates of nitromethane a) compiled from previous studies with b) a magnified view from 3 to 14 MPa.

Over the past two decades, the use of nano-scale particles to create viable nanofluid propellants has been examined extensively; these combustion studies have included synthesized alumina catalysts dissolved in JP-10 [11], aluminum powder mixed with water [12], and three-part mixtures of aluminum, water, and hydrogen peroxide [3]. However, the effects of aluminum and other additives on the specific combustion behavior of nitromethane have only recently entered the arena of study. One past report by Weiser *et al*. examined the behavior of nitromethane gelled by Aerosil 200 fumed silica and ALEX fine aluminum particles [22]. A separate study by Sabourin *et al*. examined nitromethane-based mixtures with varying concentrations of 38- and 80-nm diameter aluminum and CAB-O-SIL TS-720 fumed silica that showed measurable increases in linear burning rates for increasing additive concentrations [23]. The same group also observed the effects of nano-scale, functionalized graphene sheets on the burning rate of nitromethane, measuring marked increases in the linear burning rates of mixed samples over those of neat nitromethane [24].

In addition to the testing of suspended particle mixtures, the first study by Sabourin *et al*. [23] also sought to confirm the burning rate behavior of neat nitromethane between 3 and 15 MPa proposed by Boyer [5] and Boyer and Kuo [20]. This study resulted in a nitromethane burning rate curve that closely approximated the lower values measured in previous STB tests, asserting that the lower values represented the truly inherent burning rate of nitromethane. This newer baseline burning rate equation is provided in Eq. (5).

$$r_b[mm/s] = 0.162\ (P[MPa])^{1.23} \quad (3 < P \leq 15\ MPa) \tag{5}$$

In these endeavors, high-speed cameras were used to capture the progression of the burning surface down a clear, quartz tube. This method required direct observation of the nitromethane combustion, limiting the range of useful apparatus designs and materials to those that allowed for optical access and visual transparency. Most recently, a thesis by Warren detailed efforts to develop a new technique to estimate the linear burning rate of nitromethane without direct visual observation of the combustion process [25]. While this study was successful in laying the groundwork for the development of a static tube burner for liquid monopropellants, it was ultimately unable to reproduce the currently accepted burning rates for nitromethane found in recent STB studies performed by Boyer [5] and Sabourin *et al*. [23].

3. EXPERIMENTAL METHODS*

3.1. Strand Burner System Overview

The strand burner used in the current study consists of a cylindrical test chamber with an inner diameter of 94 mm (3.70 in.), a height of 203 mm (8.00 in.), and three optical ports surrounding the propellant test site. A single orifice centered on the top surface connects to both the inlet gas line used for pressurization and outlet gas line used for exhausting the chamber, while a larger orifice centered on the bottom surface is used to insert a custom-fabricated burner plug. This system has the ability to record the instantaneous pressure, light intensity, and electromagnetic emission spectrum of a small sample of solid or liquid propellant throughout the combustion process.

The design of this system allows researchers to remotely initiate and monitor the progress of propellant burning from a nearby control room. When active, the strand burner is separated from the control center by reinforced concrete walls, a 1.5-in. blast door, and an additional fire door. After insuring that no personnel are present within the testing area, security cameras are used to monitor against equipment failure and verify that the test cell remains empty until the strand burner has been completely vented and depressurized. Additional details regarding the strand burner hardware and attached pressurization systems may be found in the thesis by Warren [25].

---

*Part of this section is reprinted with permission from:
K.W. McCown III, A.R. Demko, E.L. Petersen, J. Propul. Power (2014) in press,
DOI: 10.2514/1.B35093, Copyright 2013 by the American Institute of Aeronautics and Astronautics;
K.W. McCown III, E.L. Petersen, Combust. Flame (2014) in press,
DOI: 10.1016/j.combustflame.2013.12.019, Copyright 2013 by the Combustion Institute.

To house the monopropellants used in the present study, a custom propellant mount was created to fit into the bottom of the strand burner. This piece was machined from a 1-in. diameter, 1.5-in. head, 3-in. long, fully-threaded, carbon steel bolt. A 0.125-in. diameter hole was drilled through one side of the bolt, housing a single strand of insulated copper wire that acted as the positive lead for an electrode. A carbon steel eyelet was installed on the end opposite from the copper wire to create the negative lead. A single, 0.358-in. diameter cavity was drilled axially between the two leads to a depth of 20 mm to house approximately 1.30 g of propellant for testing. A diagram summarizing the design of the specialized propellant mount is shown in Fig. 2.

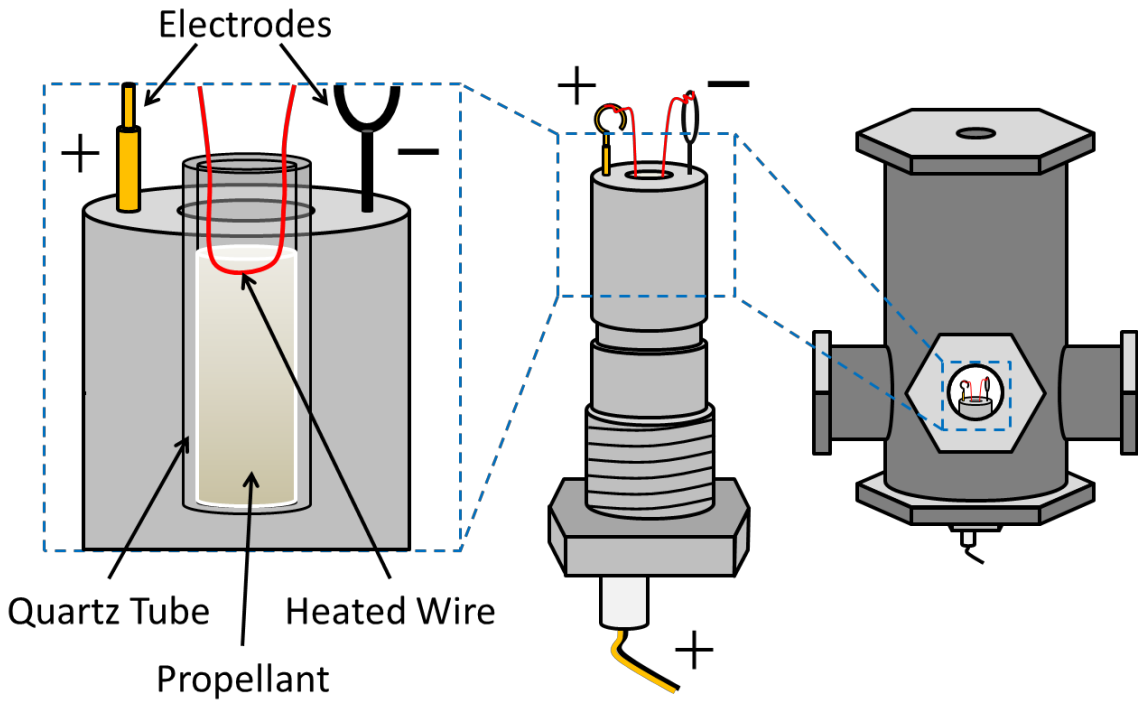

Fig. 2. Custom propellant mount used to house and ignite liquid-based monopropellants in the strand burner.

A segment of fused quartz tubing was inserted into the central mount cavity to examine the effects of different wall materials on the burning rate of nitromethane. The segment possessed an outer diameter of 9 mm and an inner diameter of 7 mm, allowing the quartz tube to snugly rest within the 9.1-mm (0.358-in) diameter cavity and house approximately 0.90 g of propellant. The tube was also sealed on one end to prevent liquid from escaping out the bottom, and a single layer of Teflon tape was wrapped around the outer surface to prevent undesired motion during testing.

A 30 gauge nickel-chromium wire was suspended in the cavity between the two electrodes and was energized via a Struthers-Dunn 0339AF electric relay connecting the propellant mount assembly to a GW Instek SPS-3610 power supply. Once the desired chamber pressure was reached, a current of 6 A was passed through the wire to heat it above 1000 °C and ignite the nitromethane sample. After ignition, the region above the propellant burning surface rapidly heated to a temperature of over 2000 °C, disintegrating the wire and allowing the sample to burn independently for the remainder of each test. This relay remained energized throughout the duration of the test, and the circuit was broken by the disintegrating nickel-chromium wire soon after ignition occurred.

The strand burner was pressurized to the desired conditions using compressed air, enabling the authors to measure the combustion behavior of nitromethane over a wide range of ambient pressures. The additional oxygen present in the air was only necessary to initialize burning; the rapid movement of the burning surface below the mouth of the cavity after ignition prevented further access to the ambient oxygen and

forced the nitromethane to burn as a monopropellant for the remainder of each test. At initial pressures below 4.5 MPa, the neat nitromethane became increasingly difficult to ignite despite the presence of air. To enable ignition at pressures below this threshold, a small pellet of solid rocket propellant comprised of ammonium perchlorate and hydroxyl-terminated polybutadiene (AP/HTPB) was threaded onto the nickel-chromium wire and ignited as a booster.

3.2. Chamber Pressures and Light Intensities

The instantaneous pressure and light intensity within the burner chamber were sampled at a 1-kHz rate by an OmegaDyne PX02C1-7.5KG5T pressure transducer and a New Focus 2031 silicon photodiode, creating a pair of ASCII-formatted files in GageScope. Both files contained sets of measured voltages versus time that could be related to the actual pressure and light intensity using calibrated conversion factors. Raw data were processed using Origin 8.07 software, where the burn time of each run was calculated graphically using the recently converted plot of pressure versus time. The overlaid pressure and light intensity traces from a typical nitromethane-based propellant trial, along with the marked start and end of combustion, are shown in Fig. 3.

To account for the transient behavior caused by the wire's initial heating of the pressurizing gas, propellant ignition was defined as the intersection of the sloped line created by the fastest rate of pressure rise with the horizontal line created by the initial chamber pressure. The end of combustion was defined as the moment when the highest chamber pressure was achieved during a test, and the slope of the pressure trace was

effectively zero. The total burning time was defined as the difference between those two events as shown in Fig. 3, while the average chamber pressure was taken from the two instantaneous pressures that corresponded to those same events.

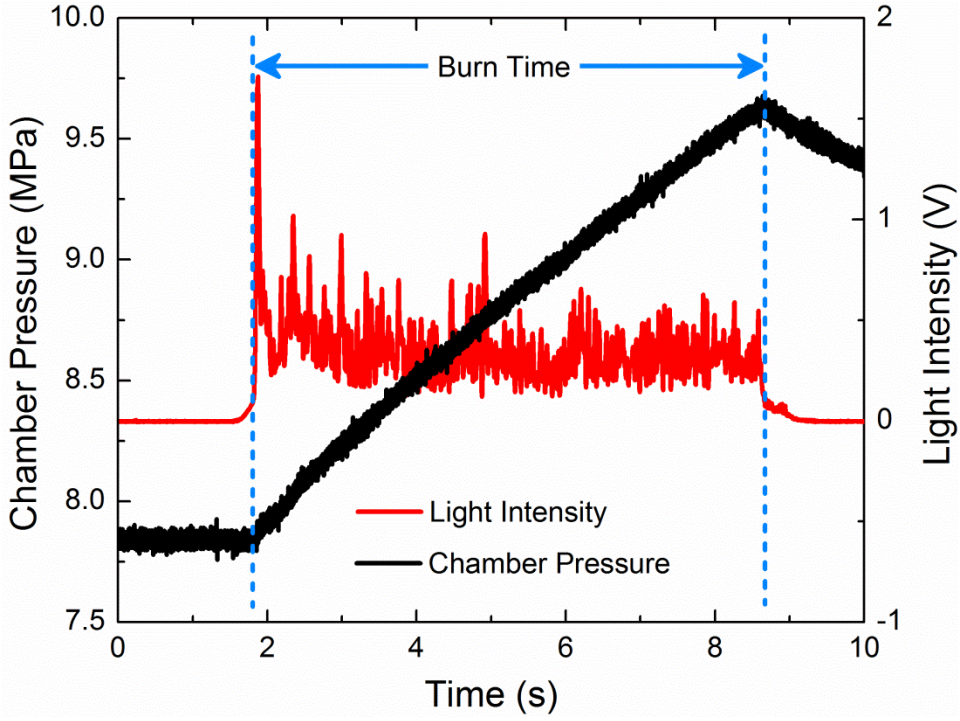

Fig. 3. Pressure and light traces for 99% nitromethane and 1% silica by weight at an average chamber pressure of 8.8 MPa with a measured linear burning rate of 2.9 mm/s. Traces are typical of all nitromethane-based mixtures used to determine burning duration and average chamber pressure.

For all trials, the start and end of combustion as defined by this method matched well with a respective increase and decrease in light intensity. The fluctuations in this light intensity trace were attributed to the turbulent behavior of the bright exhaust plume created by the motion of exhaust and pressurizing gases above the mouth of the burner

tube during combustion. Despite the unsteady values of the light intensity during the burn, the average value is shown to peak at the onset of combustion and slowly decrease as the flame front and exhaust plume move further below the mouth of the burner tube and away from the detector's line-of-sight, providing clear means of verifying the starting and stopping points of combustion.

3.3. Linear Burning Rates

With the burning time (Δt) and average chamber pressure identified from available data traces, the only remaining variable to be determined was the axial length of burned propellant (Δx). This value was calculated using the measured mass of propellant burned during each trial (m), the known propellant cavity diameter (d), and the calculated overall density of the monopropellant mixture (ρ). The burned propellant mass was determined by subtracting the residual propellant mass left after each trial from the initial propellant mass present before burning. These variables were all combined to estimate an average linear burning rate for each trial in accordance with Eq. (6).

$$r_b = \frac{\Delta x}{\Delta t} = \frac{4m/(\pi \rho d^2)}{\Delta t} \tag{6}$$

The overall densities of heterogeneous monopropellant mixtures were calculated using the known weight fractions of each constituent material (Y_i) and the known densities of each propellant component (ρ_i). Eq. (7) provides an example of this calculation for a typical four-part mixture of nitromethane, silica, aluminum, and titania as used in the current study.

$$\rho = \frac{1}{(Y_{NM}/\rho_{NM})+(Y_{SiO_2}/\rho_{SiO_2})+(Y_{Al}/\rho_{Al})+(Y_{TiO_2}/\rho_{TiO_2})} \quad (7)$$

This method was numerically equivalent to using the volumetric fractions of the propellant liquid and added particles to calculate the overall density, as is typically done for slurries.

After each trial, a small amount of propellant residue remained on the inner surface of the quartz tube inside the propellant mount. This residual mass typically varied from 0% to 3% of the initial propellant weight as a function of the particle weight percentage, with higher percentages yielding more residue. Lower initial chamber pressures—and subsequently lower burning rates—resulted in fewer exhausted particles and a greater residual weight percentage for a given mixture composition. The residual weight percentages were less than the known weight percentages of suspended particles for all tests, indicating that some particles became entrained in the exhaust plume and were ejected from the quartz tube during combustion.

Mixtures containing aluminum were more likely to have residual weights that were significantly smaller than the known particle load, likely caused by the ejection of aluminum particles during their energetic participation in propellant combustion and subsequent conversion to alumina. The residual mass present after each test was subtracted from the initial propellant mass to determine the burned mass utilized in Eq. (6). While the level of residue was likely affected by the loss of solid particles that had become entrapped in the exhaust plume, the subsequent changes to the estimated masses of propellant burned and linear burning rates were so small as to fall within the overall scatter of the collected data.

3.3. Spectroscopic Emission

Spectroscopic emission data were also collected for each trial using an OceanOptics USB2000 spectrometer, allowing the authors to examine each combusted sample for prevalent species emissions and signs of material impurities. The emission curves for neat nitromethane and a mixture containing 1% silica and 5% aluminum by weight are shown in Fig. 4 as examples of the spectral data recorded for the current study, and two typical data sets were taken at similarly high and low pressures for each mixture. While each emission spectrum represents an instantaneous snapshot from a given trial, the associated pressure value represents the average chamber pressure taken over the full duration of the same trial.

The most prominent features of the propellant spectra at high pressures were vapor lines for sodium and potassium, and the intensity of these lines relative to the overall emission curve diminished as the chamber pressure was reduced. The single sodium line centered at 589.2 nm was an amalgamation of the sodium D1 and D2 lines, while the weaker potassium lines at 766.8 nm and 770.2 nm were the slightly-shifted counterparts of the potassium D1 and D2 lines. The accepted wavelengths of the sodium emission lines were directly utilized in the calibration of the spectrometer, while the wavelengths of the potassium emission lines were not. This procedure resulted in an amalgamated sodium line whose observed wavelength fell between the accepted values of the separate lines, while the observed wavelengths of the potassium lines only drifted by 0.3 nm over the 177-nm gap between line groups.

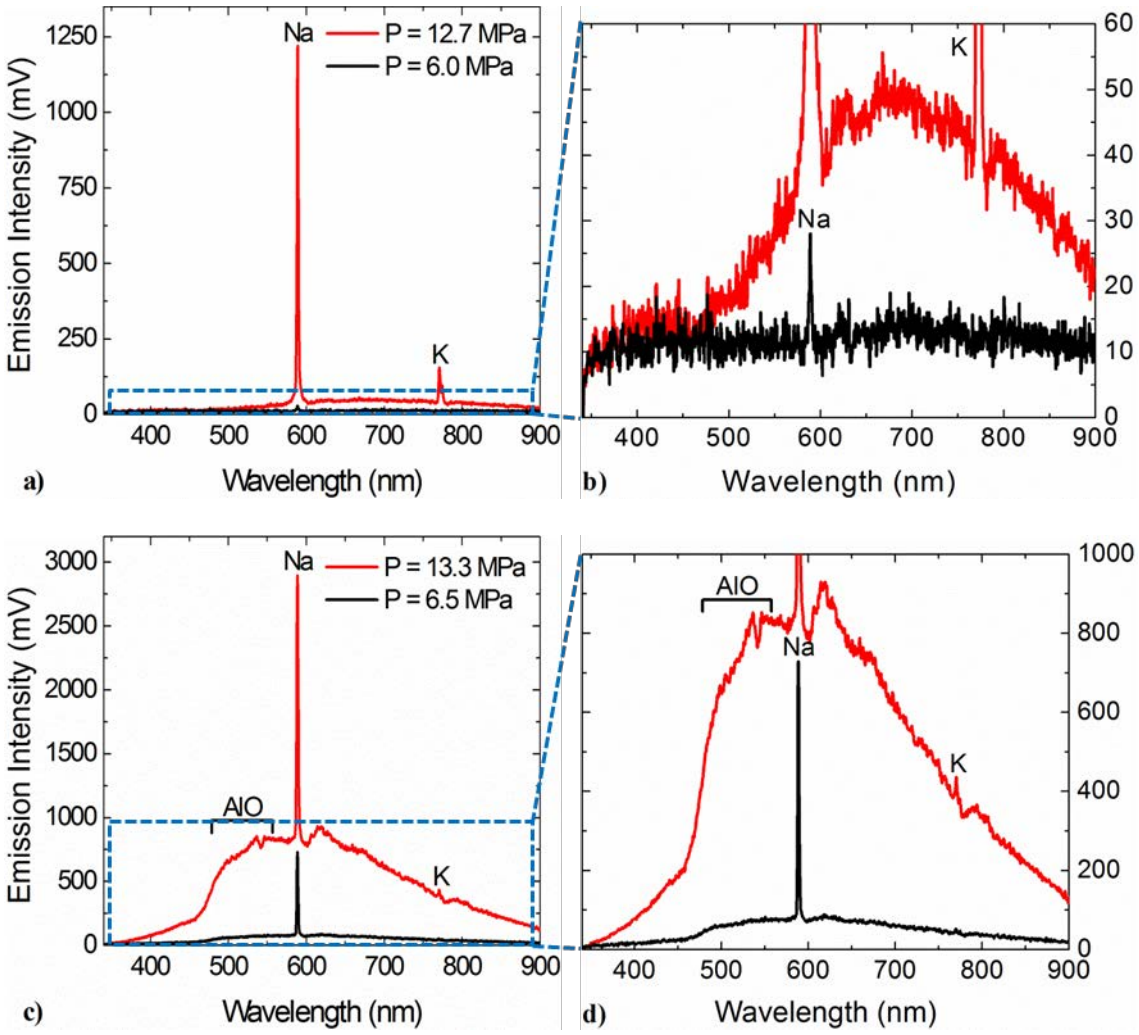

Fig. 4. Emission spectra at high and low average chamber pressures: a) neat nitromethane, b) magnified view of nitromethane, c) mixture with 1% silica and 5% aluminum, and d) magnified view of mixture.

These contaminants have appeared in the emission spectra of a variety of solid and liquid propellants tested by other research groups, where their unintended presence was reported to not have any significant impact on propellant performance [26-28]. For the current study, these elements were thought to have been introduced during the

manufacture of the nitromethane, where nitrite salts containing both sodium and potassium are often used in the large-scale production of the chemical.

A previous study of combustion emission spectra by Petersen *et al*. characterized the blackbody emission response of authors' current spectrometer system with a quartz-tungsten-halogen (QTH) lamp [27]. The two broad peaks that consistently appeared at 650 nm and 800 nm in all propellant trials from Fig. 4 also appeared in the QTH emission curve in the previous study, indicating that these features were caused by the properties of the spectrometer system and not any particular combustion species. The tapering of the broadband emission at lower and higher wavelengths was also due to the spectral response of the spectrometer that was used [27].

The addition of silica and aluminum produced emission spectra whose intensities were much greater than those for neat nitromethane at any given chamber pressure. In particular, the relative intensity of the emitted light from 430 to 550 nm was increased significantly when compared to the overall shape of the emission curve for nitromethane alone. This region of increased intensity shared the same wavelengths as the blue-green emission band for aluminum (II) oxide previously observed by Goroshin *et al*. for aluminum dust premixed with air [28]. Its presence, as anticipated, indicated that aluminum combustion had occurred when testing the mixture containing 1% silica and 5% aluminum by weight and was also observed for other mixtures containing greater quantities of aluminum.

3.4. Nanoparticle Additives

The nitromethane used in the current study was designated as reagent grade as defined by the American Chemical Society and guaranteed to be at least 95% pure by its manufacturers at Sigma-Aldrich Co. Aluminum nanoparticles with a mean diameter of 100 nm were purchased from US Research Nanomaterial, Inc.; a reported specific surface area of 10 to 20 m^2/g corresponded to the individually spherical aluminum particles. Particles of this size and morphology are widely available on the commercial market and enable comparisons to be made between future studies completed using these particles and the previous study completed by Sabourin *et al*. using similar, 80-nm particles [23].

Previous studies of particle suspensions in nitromethane indicated that similarly sized aluminum particles were difficult to suspend without an additional thickening agent, with silica powder serving as the unanimous thickener of choice [22,23]. Fumed silica powder consisting of 200- to 300-nm aggregate particle chains with an amorphous crystalline structure was chosen as the thickening agent for the current study and purchased from Sigma-Aldrich Co. A specific surface area of 200 m^2/g was reported by the manufacturer and corresponded to the aggregate chains of silica.

Titania nanoparticles with a mean diameter of 20 nm and an amorphous crystalline structure were purchased from Mach I, Inc. and chosen as the final additive for the current study. An average specific surface area of 148 m^2/g was reported by the manufacturer and corresponded to the individually spherical titania particles.

Transmission Electron Microscopy (TEM) images of these three nanoparticle additives are provided in Fig. 5.

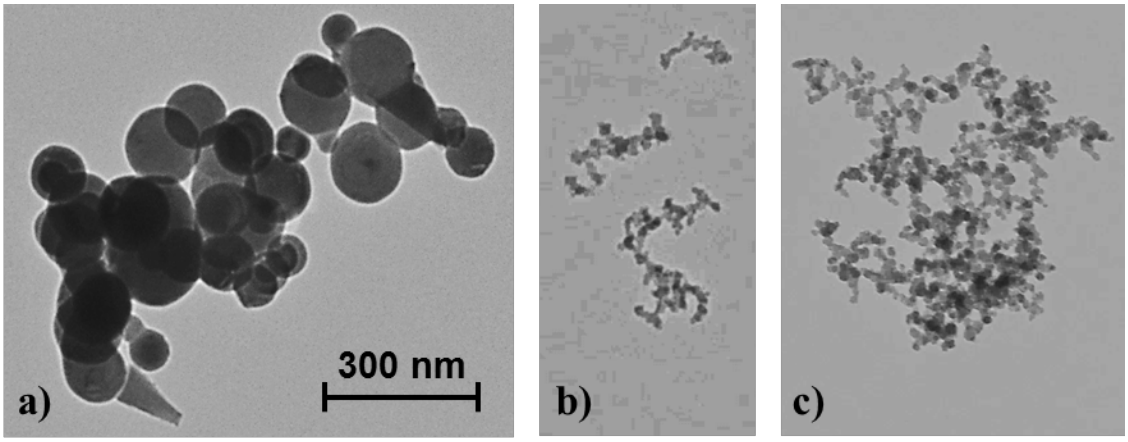

Fig. 5. TEM images of nano-scale particle additives: a) aluminum, b) fumed silica, and c) titania.

To obtain these images, the aluminum and silica nanoparticles were separately added to nitromethane at a highly diluted level of 0.1% by weight to reduce particle crowding and allow for the imaging of individual agglomerates. After a brief period of mixing by hand, microliter-sized quantities of each suspension were deposited on carbon mesh grids where the nitromethane was allowed to evaporate off under ambient conditions prior to imaging under the TEM. While the fundamental size of the aluminum and titania nanoparticles did match the expected 100- and 20-nm sizes, these individual particles were consistently entangled in larger agglomerates that could be up to several microns across. On the other hand, the size and configuration of the silica nanoparticles closely matched those of the expected 200- to 300-nm aggregate chains. The common

presence of aluminum and titania agglomerates indicated that additional efforts were needed to ensure the creation of quality propellant mixtures whose particle sizes matched expectations.

3.5. Nanoparticle Settling Study

The nitromethane and dry powders were individually weighed using an Ohaus ARA520 digital scale with a resolution of 0.01 g to determine the weight percentages of each constituent material. An excessive 50 g of nitromethane were used as the base for each mixture, diminishing the relative weight loading error caused by the limited scale resolution and decreasing the likelihood of sunken agglomerates being drawn up during sample extraction. It is useful to note that the aluminum weight percentages reported in the current study are inclusive of any oxide coating.

To further ensure that the measured burning rates were not affected by particles that had settled over time, propellant mixtures were combined and agitated just prior to testing. A Sper Scientific, Ltd. 100004 ultrasonic mixer was used for at least 25 minutes before each test to encourage even mixing at 42 kHz, breaking apart these existing agglomerates and preventing the development of new clusters. Afterward, a plastic pipette was used to load the mixture into the central cavity of the propellant mount before insertion into the strand burner. Even without any widespread agglomerations, some particle mixtures were simply unable to remain suspended for enough time to be reliably tested.

A study was completed to measure the longevity of each particle suspension and the weight percentage of particles that had not yet settled to the bottom of the mixture volume, guaranteeing that no tested mixtures would settle in the few minutes between loading and ignition. After the initial ultrasonic mixing period, each nanofluid was briefly agitated by hand but left undisturbed for the remainder of the settling study. At various intervals of time, a large pipette was used to draw liquid from a depth slightly below the surface of the mixture volume. The same drawing depth was used for each subsequent time interval, and each liquid sample was deposited into separate glass beakers.

The initial sample weight was measured using the same Ohaus digital scale, and the samples were allowed to fully dry overnight under the reduced atmospheric pressure of an evacuated desiccator. The final weight of each dried sample was then compared to its respective initial weight, revealing the weight percentage of the solid material that had originally been suspended and subsequently drawn up with the extracted nitromethane. Several settling curves representing both stable and unstable nanofluids are provided in Fig. 6 to summarize the results of this study.

The nearly horizontal curves of the mixtures that contained both silica and aluminum indicated stable particle suspensions that could be reliably tested, while the decaying curves of the mixtures that contained only aluminum confirmed the reports of previous groups who concluded that an additional thickening agent was required to ensure repeatable trials with larger-diameter aluminum particles [22,23]. The relatively high surface areas of the smaller silica and titania nanoparticles allowed these additives

to act as effective gellants, while the chain-like structure of fumed silica aggregates have been shown to promote thixotropic behavior in nitromethane-based nanofluids [29]. While not exhaustively represented in Fig. 6, all tested mixtures were first determined to be stable in this manner before combustion testing in the strand burner took place.

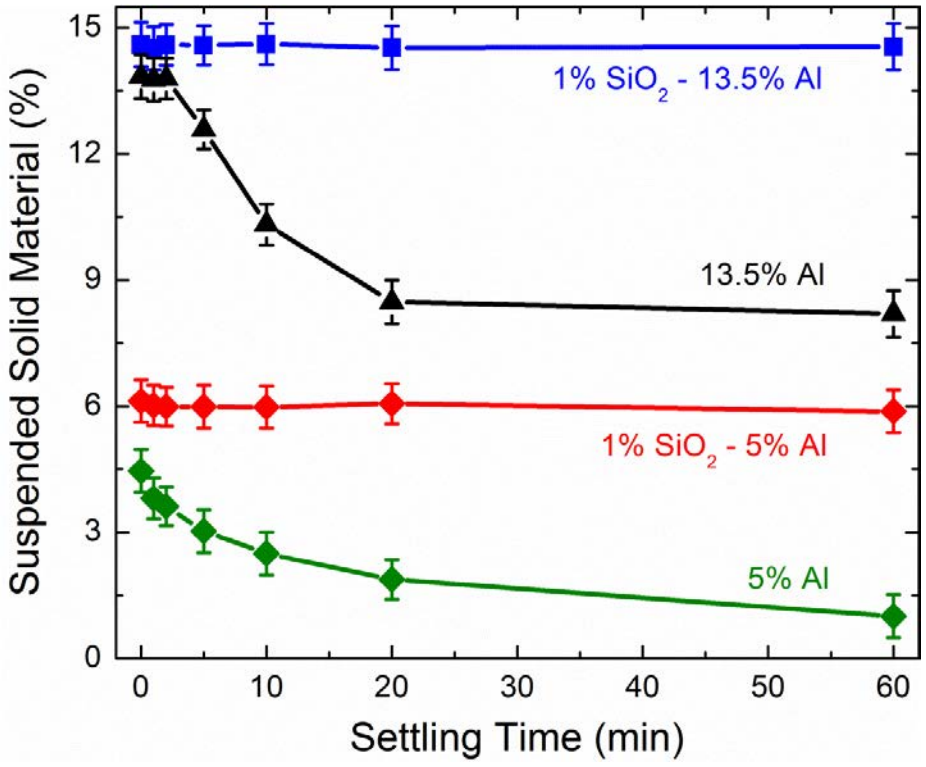

Fig. 6. Weight percentages of suspended particles as functions of settling time for select mixtures of nitromethane, aluminum, and silica.

3.6. Measurement Uncertainty

The primary source of measurement uncertainty in the current study was the small difference between the actual propellant ignition time and the ignition time estimated from the type of pressure trace shown in Fig. 3. Because of inherent signal

noise, the horizontal and sloped lines used to estimate the start of combustion were drawn through the center of the fluctuating pressure trace for each trial. However, similar horizontal and sloped lines could be drawn though the upper or lower limits of the oscillating data to indicate a slightly faster or slower ignition delay. While the use of centered lines provided a consistent treatment of the pressure data, there was no way to pinpoint the exact start of combustion within the bounds of this signal noise.

By assuming a worst-case scenario where the actual ignition was as far away from the perceived central point as possible, small burning time uncertainties that ranged from ±0.02 to ±0.29 s were created for burn times that ranged from 0.5 to 26 s. The absolute size of the burning time uncertainty was proportional to the overall burning time, and its values were combined with a resolution error of ±0.005 g for the digital scale used to measure propellant masses to define a total measurement error that varied from 2% to 8%. The measurement uncertainty of the settling study was also a result of the resolution of the digital scale used to weigh each sample; the maximum and minimum error bar values seen in Fig. 6 correspond to estimated particle weight percentages from initial and dried sample weights that oppositely deviated from the recorded vales by the aforementioned scale resolution error.

4. RESULTS AND DISCUSSION*

4.1. System Sensitivity and Nitromethane Baseline

An initial sensitivity analysis determined how changes in the input parameters affected the burning rate of a given monopropellant as measured using the author's system. The chosen parameters for analysis consisted of the initial mass of the propellant, wetted length of the nickel-chromium wire, material of the central cavity walls, and oxygen concentration of the pressurizing gas. The input parameters were separately varied at numerous initial pressures to prevent any bias that could result from the singular focus on any one pressure, as described next.

The initial mass of the propellant was varied by altering both the volume of propellant deposited into the central cavity and the actual depth of the cavity drilled into the propellant mount. These changes resulted in axial propellant lengths that varied from 10 to 20 mm, changing the distance from the propellant surface to the cavity mouth and the availability of ambient oxygen for the nitromethane before burning. Varying the wetted length of the nickel-chromium wire from 9 to 25 mm altered the amount of heat energy dissipated into the quiescent nitromethane, slightly changing the initial temperature of the liquid. The material of the central cavity walls adjacent to the propellant was changed from carbon steel to fused quartz by inserting the previously

---

*Part of this section is reprinted with permission from:
K.W. McCown III, A.R. Demko, E.L. Petersen, J. Propul. Power (2014) in press,
DOI: 10.2514/1.B35093, Copyright 2013 by the American Institute of Aeronautics and Astronautics;
K.W. McCown III, E.L. Petersen, Combust. Flame (2014) in press,
DOI: 10.1016/j.combustflame.2013.12.019, Copyright 2013 by the Combustion Institute.

described quartz tube segment. The oxygen concentration of the pressurizing gas was varied by partially filling the strand burner to 50% or 75% of the desired initial pressure with air and filling the remainder with inert argon.

For trials performed with the exposed carbon steel propellant mount, the measured burning rates of nitromethane in the current study closely matched elevated rates from the previous study by Warren [25] and the LFB study by Boyer [5]. The elevated rates seen in these studies belonged to the faster of two apparent burning rate trends found for nitromethane between 3 and 15 MPa, while the additional STB study by Boyer [5] revealed a significantly slower burning rate trend for the same pressure range that was later confirmed by Sabourin *et al*. [23]. The slower trend has since been accepted as the inherent burning rate equation for nitromethane, while the cause of the faster burning rate trend was attributed to systematic errors by the respective authors but never pursued beyond speculation.

Performing the initial sensitivity analysis of the current testing configuration without the added quartz segment simplified the testing process and better enabled a large number of trials. It also allowed the present study to focus on the more subtle effects of changing parameters other than the cavity wall material. Figure 7 displays the data collected during this sensitivity analysis and compares it against the elevated burning rates seen in previous studies by other researchers. A complete record of the chamber pressures and linear burning rates for all propellant mixtures measured in the current study is included in Appendix B.

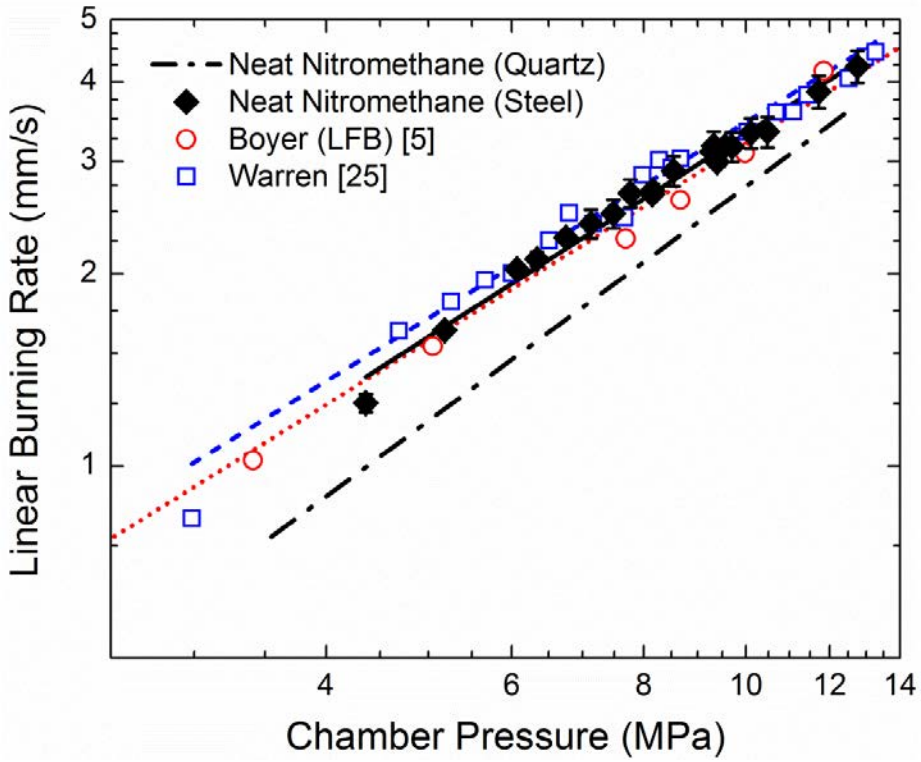

Fig. 7. Sensitivity analysis and measurement uncertainty of nitromethane burning rates in the carbon steel cavity compared with recent studies from literature [5,25].

The measurement uncertainty of each burning rate was represented by vertical error bars and defined by the aforementioned interpretation of the typical pressure trace shown in Fig. 3. These error bars are present for all burning rate data presented herein, but their small magnitudes cause them to be obscured by the symbols of most data points. The low scatter showed that changes in the axial propellant length had no effect on the burning rate trend of nitromethane, validating the assumption that the propellant can be treated as a one-dimensional system in the current burner setup. A previous study by Boyer *et al*. [18] showed that large changes in the initial temperature did have some small effect on the burning rate of nitromethane and its resulting rate equation, but the

consistent data trend in Fig. 7 indicated that any temperature changes caused by the different wire lengths in the current study were at least smaller than those temperature variations encountered by Boyer *et al*.

Interestingly, reducing the partial pressure of air to 50% or 75% made the nitromethane impossible to ignite at all but the highest pressures without the previously unnecessary solid booster. Despite the use of the added booster pellet, the measured burning rates still fell on the same trend line as before. While the previous study by Warren utilized a pressurizing atmosphere of 21% oxygen and 79% argon in all trials, most burning rates from the current sensitivity study in Fig. 7 were measured in an atmosphere of roughly 21% oxygen and 79% argon present within the standard mixture of compressed air. The high degree of consistency between these two datasets proved that the disparate thermodynamic properties of argon and nitrogen had not affected linear burning rates when the oxygen concentration remained unchanged; tests with reduced oxygen concentrations were similarly unaffected by the separate presence of these different gases.

In the end, the only tested parameter that had any significant effect on the burning rate and subsequent rate equation of nitromethane was the material of the cavity wall. By inserting the quartz segment into the steel cavity, the measured burning rates in the current study dropped dramatically and conformed to the lower rates reported by Sabourin *et al*. [23] and Boyer [5] for their STB tests. The substantially higher burning rates within the carbon steel cavity could be attributed to one of two possibilities: the enhanced thermal diffusivity of the carbon steel walls redirecting thermal energy from

the reaction zone to preheat the quiescent nitromethane, or the carbon steel walls taking place in a catalytic reaction with nitromethane to accelerate the burning process. Adding an insulating layer of fused quartz on top of the carbon steel wall either decreased the thermal diffusivity to prevent significant preheating or simply prevented a catalytic reaction between the nitromethane and carbon steel from occurring altogether. The known temperature sensitivity of nitromethane explored by Boyer *et al*. [18], along with the known catalytic effect of stainless steel and other materials on nitromethane shown by Kindsvater *et al*. [30], gave credence to either possibility.

Further testing focused on establishing a definitive burning rate equation for nitromethane to evaluate the results of the newly developed technique against those gathered by previous groups using an STB. These measurements were made using the same propellant mount and strand burner system, and the quartz segment shown in Fig. 2 was added to prevent the accelerating effect of the carbon steel walls and better match the systems of other researchers. Figure 8 illustrates this baseline study and also includes the results of studies by Boyer [5] and Sabourin *et al*. [23] that utilized quartz tubes and optical measurements for direct comparison.

The burning rates measured in the current study closely matched those actually observed in previous optical systems, despite the lack of any direct visual observation in the author's method developed for the current study. The consistency of this technique was exhibited in the extremely low scatter of the data, further validating the use of the authors' method when determining the linear burning rates of monopropellants such as nitromethane.

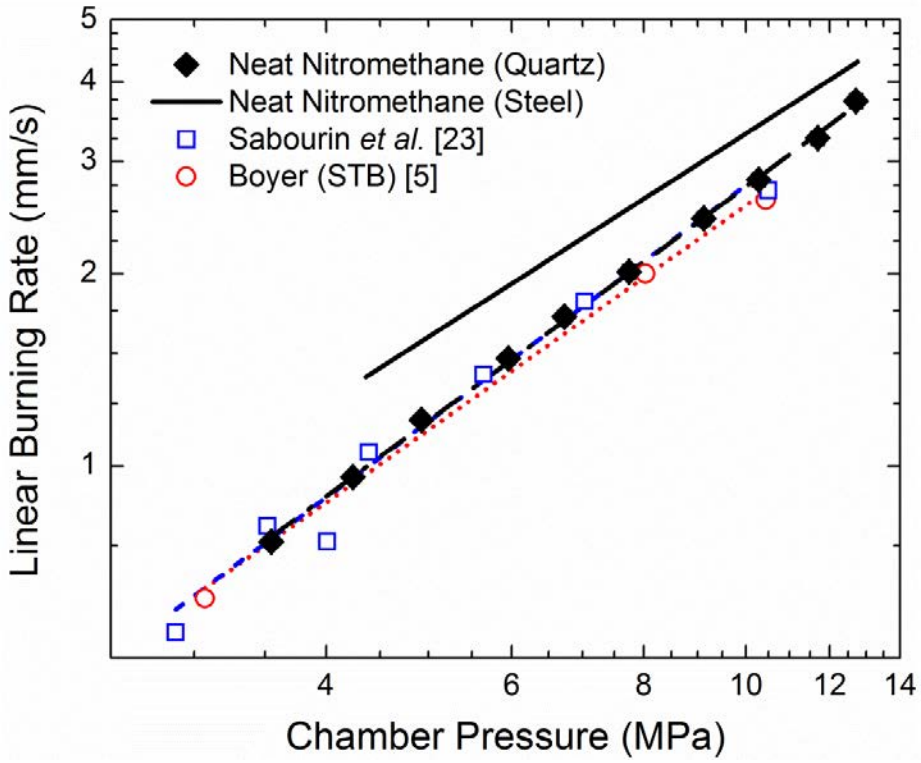

Fig. 8. Linear burning rates of nitromethane inside the fused quartz segment compared with studies completed in quartz tubes equipped with optical systems [5,23].

Several complete pressure traces were input into a computer program detailed in the thesis by Frazier to show that the average burning rate taken across the entire pressure range for each baseline trial was a valid estimation at each average pressure [31]. This program utilized a mathematical model of the current strand burner facility at Texas A&M University and the raw pressure-time history to calculate a set of instantaneous burning rates based on smaller subsections of the overall data trace. For all tested data sets, the instantaneous burning rate estimates began at a slightly lower value than the average burning rate and increased until they were slightly greater than the average value. This result was expected, because the instantaneous chamber pressure

began at a slightly lower value than the average pressure and increased until it reached some maximum slightly above the same average value.

Despite the differences between estimated instantaneous values and measured average values, the use of chamber pressures and burning rates that were averaged across the entirety of each trial resulted in burning rate curves that closely matched those produced by other research groups using instantaneous data. This excellent agreement between the results of the simplified method used in the current study and the trends observed by other researchers using a high-speed camera proved that this approximation was a good representation of the actual system behavior despite the actual presence of transient chamber pressures and subsequent burning rates.

4.2. Heat Transfer Models

To identify the true source of disparity between the burning rates of neat nitromethane surrounded by either fused quartz or carbon steel walls, two simplified analytical models and a numerical approximation of the strand burner cavity were created in MATLAB. The models and numerical approximations produced separate, transient temperature profiles for the fused quartz segment and carbon steel propellant mount using separate, one-dimensional modes of heat transfer in the radial and axial directions. Figure 9 illustrates the primary axes and boundary conditions of both heat transfer modes for the most recent configuration of strand burner materials.

In the analytical models, the quartz and steel burner tubes were separately represented; the radial systems contained either the individual quartz or steel component

whose dimensions are described in Fig. 9, while the axial systems contained a full 90 mm of either the quartz or steel instead of the layered configuration shown in the same figure. Several assumptions were made to establish the boundary conditions of the heat transfer models and simplify them to a degree that allowed a single equation to describe each time-dependent temperature distribution.

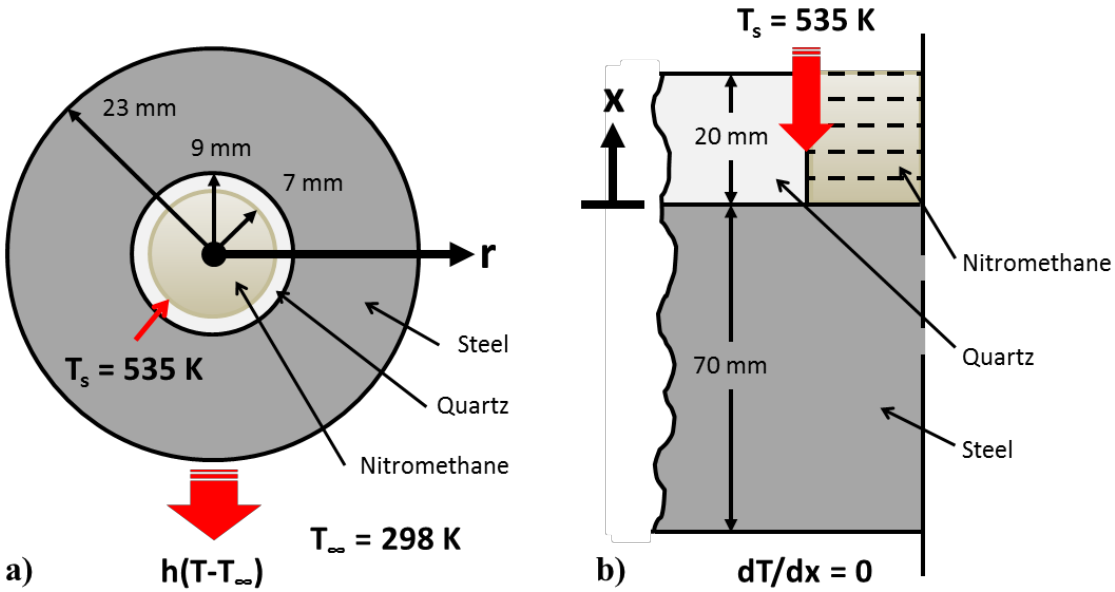

Fig. 9. Primary axes and boundary conditions heat transfer modes for the combined quartz and steel strand burner tube configuration: a) radial and b) axial.

For the radial heat transfer model, the temperature of the inner cavity surface was set at a constant 535 K, while the outer surface was allowed to convectively cool using the room-temperature air within the strand burner. For the axial heat transfer model, the temperature of the cavity wall adjacent to the nitromethane burning surface was set at a constant 535 K, and the exposed bottom of the propellant mount was assumed to be an

adiabatic boundary. The temperature gradient at the base of the 90-mm steel mount or equivalent quartz tube was nearly nonexistent, and the local temperature there remained within 0.1 K of the initial temperature during the longest modeled time interval; this observation supported the use of an adiabatic boundary condition in the axial model and greatly simplified its defining equation. The constant-temperature boundaries in both models were based on a recent model of nitromethane combustion created by Boyer and Kuo, where 535 K corresponded to the surface temperature of burning nitromethane at 3 MPa [32].

While the analytical models directly described the transient temperature profiles of the steel propellant mount used in the current study and the quartz tube used by other researchers, the layered system of quartz inside steel also used in the current study was most readily described by a numerical approximation based on the explicit finite-difference method. To account for heat transfer between the fused quartz segment and original carbon steel mount, both the radial and axial approximations incorporated distinct layers of quartz and steel that shared a perfect thermal contact surface and are shown in Fig. 9. These numerical approximations utilized the same outer boundary conditions as the analytical models, and their accuracy was verified against the predictions of the analytical models to within 0.043% by approximating the separate steel and quartz configurations.

The initial temperature of nitromethane has been shown to have the greatest impact on its linear burning rate at lower chamber pressures; assuming a pressure at the low end of the desired range produced temperature profiles for the burner tube that

corresponded with this enhanced sensitivity [18]. The effects of heat transfer on the opposite side of the isothermal boundaries were not accounted for in the simplified models or approximations; instead, the current algorithms only examined the temperature and material effects from the regions between the two sets of stated boundary conditions. While these simplifications did prevent the current models from comprehensively describing the heat transfer characteristics of the entire strand burner system, these algorithms were created only to identify whether or not the differing thermal characteristics of the cavity materials allowed the initial temperature of quiescent nitromethane to significantly vary enough to account for the disparate burning rate curves.

The radial position (r), time (t), temperature of the propellant burning surface (T_s), thermal diffusivity of the burner tube material (α), and radii at burner material boundaries (r_i) are included in Eq. (8) to define the radial temperature profile of the burner tube as a function of time [33].

$$T(r,t) = T_s + \sum_{i=1}^{\infty} \frac{1}{N(\beta_i)} e^{-\alpha\beta_i^2 t} R_0(\beta_i, r) \int_{r_1}^{r_2} r R_0(\beta_i, r) F dr \tag{8}$$

Similarly, the axial position (x) and burner tube length (L) are included in Eq. (9) to define the axial temperature profile of the burner tube as a function of time [33].

$$T(x,t) = T_s + \sum_{i=1}^{\infty} \frac{1}{N(\beta_i)} e^{-\alpha\beta_i^2 t} X(\beta_i, x) \int_{0}^{L} X(\beta_i, x) F dx \tag{9}$$

The norms (N), eigenfunctions (X), eigenvalues (β), and initial temperature functions (F) for both heat transfer models are unique to each system and further elaborated upon in Appendix A.1. The explicit finite-difference formulas used to approximate these same modes of heat transfer for combined quartz and steel systems are provided in Appendix

A.2. The radial temperature profiles of a lone quartz tube similar to those used by other researchers, along with the carbon steel mount and layered configuration used in the current study, are compiled in Fig. 10.

The greater thermal diffusivity of the carbon steel mount resulted in higher temperatures near the inner cavity surface for nearly the first second of exposure to the burning surface temperature, but the reduced thickness of the lone fused quartz segment allowed it be more effectively heated over longer time intervals. By fitting the quartz segment within the steel cavity, the material temperatures at all radii were lower than those of both quartz and steel when separate.

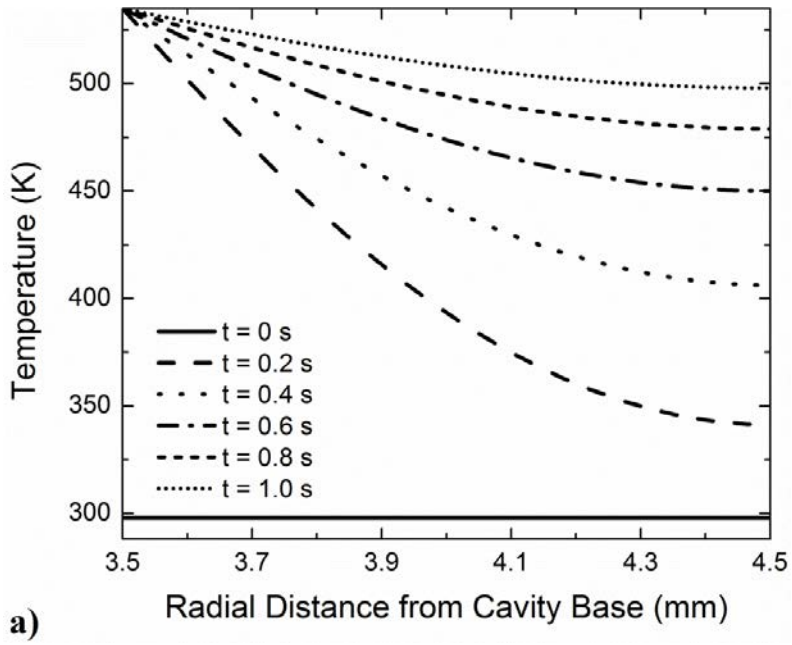

Fig. 10. Transient temperature profiles for radial heat transfer through strand burner tubes: a) fused quartz segment, b) carbon steel mount, and c) combined layers.

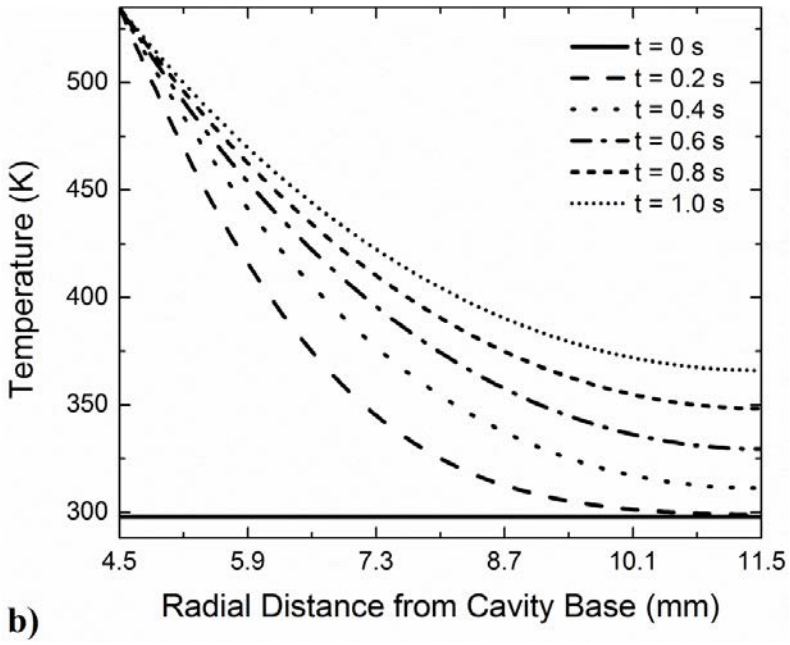

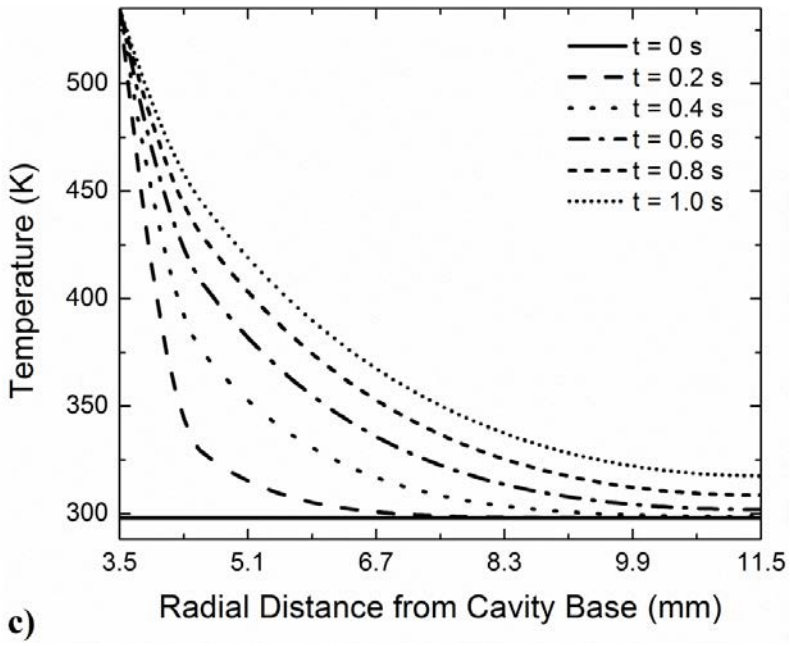

Fig. 10. Continued.

The boundary surface temperatures (T_i) of the inner cavity and outer tube surface were taken from these models at various time steps and combined with their thermal

conductivities (k_i) in Eq. (10) to estimate the radial heat transfer rates per unit length (q') for both cavity materials.

$$q' = \frac{2\pi(T_1 - T_3)}{ln(r_2/r_1)/k_Q + ln(r_3/r_2)/k_S} \tag{10}$$

For those temperature profiles based on a single tube material, the one pair of boundary radii were given the same value and used to eliminate the irrelevant term from the denominator. The radial heat transfer rates per unit length taken from Eq. (10) were recorded at several time steps and plotted in Fig. 11 for comparison.

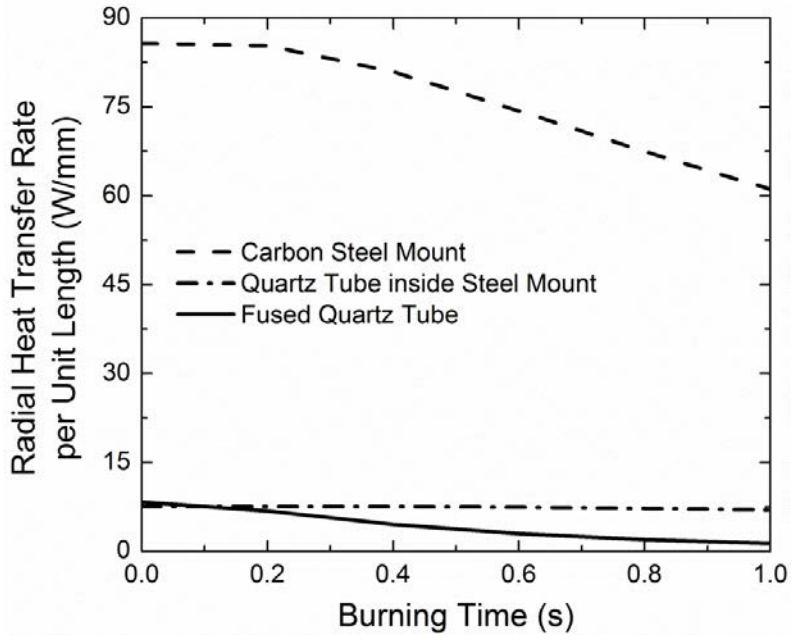

Fig. 11. Radial heat transfer rates through fused quartz segment, carbon steel mount, and combined layers as functions of time.

The higher radial heat transfer rates achieved by the carbon steel mount were expected to pull greater amounts of thermal energy away from the nitromethane within

the burner cavity than the systems that included quartz, thereby reducing the initial propellant temperature and decreasing the linear burning rate. Both the lone quartz segment and layered combination significantly reduced the rate of heat transfer away from the propellant cavity, but the smaller temperature gradient of the lone quartz segment seen in Fig. 10 helped to reduce its heat transfer rate further. The diminished radial heat transfer losses of those systems containing quartz should have led to higher linear burning rates, yet the improved burning rates of nitromethane with carbon steel in Fig. 7 indicated that this intuitive relationship did not govern the propellant behavior in the authors' current system. Instead, those empirical measurements pointed to a different cause for the shift in linear burning rates between cavity materials, namely a catalytic reaction between nitromethane and carbon steel.

The axial temperature profiles of the same fused quartz tube and carbon steel mount were created using Eq. (9) and compiled for comparison in Fig. 12. The time intervals chosen for each plot reflected the burning time required for 10%, 20%, 40%, 60%, and 80% of the propellant length to be consumed using both tube materials, and the faster burning rates of nitromethane in carbon steel resulted in smaller time steps. The decreased thermal diffusivity of the fused quartz segment yielded lower temperatures than the carbon steel mount for all axial positions below the nitromethane burning surface, but this difference shrank as the burning surface moved toward the base of the burner cavity. Unlike in the radial heat transfer model, the higher temperature of the carbon steel wall ahead of the burning surface did allow for greater heat transfer into the quiescent nitromethane, increasing the initial temperature of the unburned propellant.

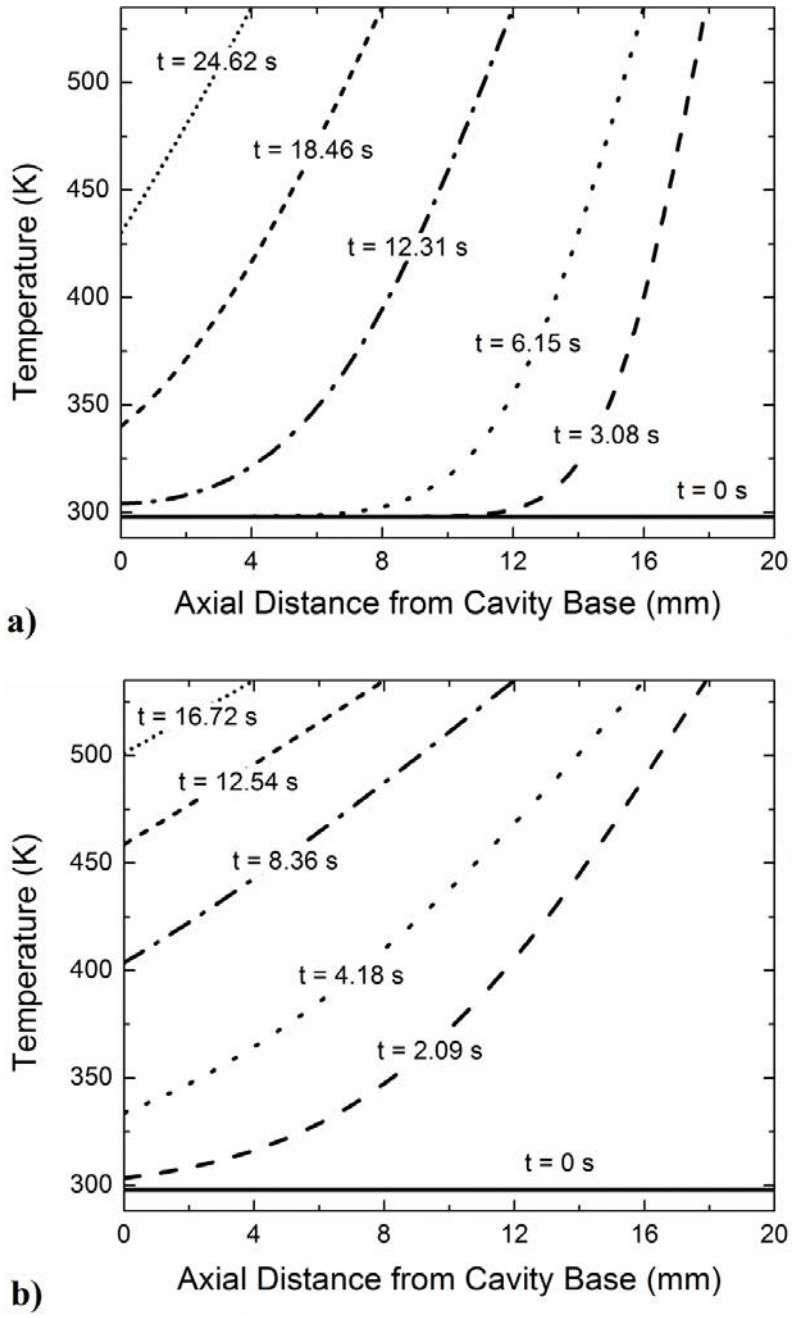

Fig. 12. Transient temperature profiles for axial heat transfer through burner tubes: a) fused quartz tube and b) carbon steel mount.

While a numerical approximation of the current quartz-steel layered configuration was also completed, the axial temperature profiles in the cavity region did not significantly differ from those of only quartz at any of the evaluated time intervals. For larger time intervals where the burning surface approached the cavity base, the combination of a 20-mm quartz segment and the remaining 70 mm of the steel mount led to cavity wall temperatures that were slightly higher than those seen with 90 mm of quartz alone.

The previously cited temperature sensitivity study by Boyer *et al*. identified a series of linear relationships between the propellant temperature (T_p) and the natural logarithm of the linear burning rate at five pressures that ranged from 2.51 to 9.96 MPa [18]. By performing a logarithmic fit of each relationship term as a function of the reported chamber pressure, the current authors were able to generate a general correlation to estimate the linear burning rate of nitromethane as a function of both initial temperature and chamber pressure. It is important to note that the correlation was based solely on the previous work by Boyer *et al*. and was not developed using data from the current study [18]. This overall correlation is shown in Eq. (11) and was used to estimate the effects of initial temperature on the burning rate of nitromethane at a specific chamber pressure of 3 MPa in Eq. (12).

$$ln\, r_b = (-2.508 + 1.538\, ln\, P) + (0.0045 - 0.0017\, ln\, P)T_p \tag{11}$$

$$ln\, r_b = -0.818 + 0.0026T_p \tag{12}$$

This correlation made it possible to estimate herein the burning rate of nitromethane at any of the numerous temperatures along each axial profile, effectively

quantifying the expected increase in burning rates from axial heat transfer when moving from fused quartz to carbon steel cavities at 3 MPa. To emphasize the effects of these differing axial temperature profiles, the axial position where the greatest temperature difference occurred was used to set the initial conditions in the two cavities. In lieu of specific data regarding the Reynolds number and other convective properties of the burning nitromethane at 3 MPa, the modeled cavity wall temperature was used to define the propellant temperature and estimate the instantaneous burning rate. The relative differences between the burning rates estimated using the wall temperatures from the axial model and the burning rates actually measured for the fused quartz and carbon steel cavities are compiled in Table 2 for comparison.

While the higher wall temperatures taken from the carbon steel model did result in elevated burning rates, the relative difference between the estimated rates were consistently smaller than what was empirically measured for both cavity materials. Furthermore, this model did not consider any radial heat losses to the burner tube or atmosphere; the elevated radial heat transfer rates for steel in Fig. 11 indicated that their inclusion would have detrimentally affected the wall temperature for the carbon steel cavity to a greater extent than the fused quartz segment. This tendency for the heated carbon steel near the inner surface to lose more heat in the radial direction would have brought the axial temperature profiles of the quartz and steel closer together, further reducing the relative differences between burning rates caused by the nearby wall temperature alone.

Table 2. Relative differences between measured and estimated burning rates at 3 MPa.

Propellant Length Consumed (%)	Axial Position of Greatest Discrepancy (mm)	Fused Quartz Wall Temperature (K)	Carbon Steel Wall Temperature (K)	Estimated Burning Rate Difference (%)	Measured Burning Rate Difference (%)
10	14.0	323	445	37.2	
20	10.5	323	445	37.2	
40	4.2	324	445	37.1	46.9
60	0	340	459	36.2	
80	0	430	501	20.2	

The combined results of the radial and axial heat transfer models showed that, while the quiescent nitromethane may have been preheated more by the cavity walls in the carbon steel mount than in the fused quartz segment, this preheating was not enough to account for the drastic increase in the observed linear burning rates. Instead, the increased rates were most likely caused by a combination of heat transfer and active catalysis between nitromethane and the carbon steel cavity.

4.3. Initial Tests on Heterogeneous Mixtures

The next series of propellant tests briefly examined the effects of aluminum and silica particles on the burning rate of nitromethane and determined if the method developed for the current study could successfully measure the behavior of these nanofluid mixtures. These measurements were completed using both carbon steel and fused quartz as cavity materials, yielding the burning rate curves shown in Fig. 13.

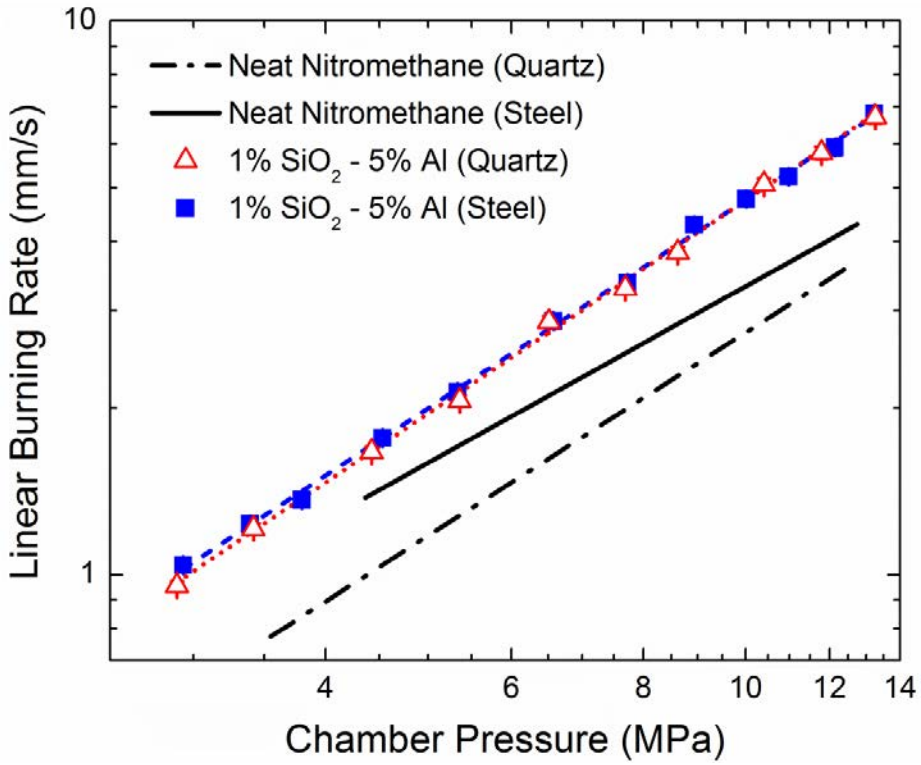

Fig. 13. Linear burning rates of nitromethane with 1% silica and 5% aluminum in metal and quartz cavities.

The burning rate curves for the mixtures in both the carbon steel and fused quartz cavities were nearly identical, despite the significant changes in burning rates that had occurred with neat nitromethane. The added 5% aluminum and 1% silica by weight acted as burning rate accelerants, overshadowing the combined heat transfer and catalytic effects of the carbon steel walls seen in Fig. 7. The mechanisms behind these accelerated nanofluid burning rates are subsequently discussed in Section 4.4. The added silica and aluminum led to linear burning rates that were 61% to 77% higher than those for nitromethane in quartz and 14% to 53% higher than those for nitromethane in steel. It is also useful to note that the nitromethane mixture containing aluminum and silica was

able to ignite at all tested pressures without the need for additional boosting, unlike the baseline of neat nitromethane. The low parameter sensitivity of these initial trials with aluminum and silica mixtures, combined with their very low data scatter, proved that the author's method also accurately measures the linear burning rates of heterogeneous monopropellants.

4.4. Mixtures Containing Silica and Aluminum

With the successful demonstration of the author's ability to reliably measure the linear burning rates of both neat nitromethane and nitromethane-based nanofluids, a series of tests were completed to characterize the effects of nano-scale aluminum, fumed silica, and titania on nitromethane combustion. The first round of nanofluid tests utilized a consistent 1% loading of fumed silica by weight to enable suspension of the aluminum nanoparticles; this silica loading was shown to be necessary by the aforementioned settling study. To isolate the effects of this silica base from those caused by subsequently added aluminum particles, a complete burning rate curve was created for a mixture that contained only nitromethane and 1% silica by weight.

This behavior was compared to the burning curves of two other mixtures containing an additional 5% and 13.5% loading of aluminum by weight. The maximum 13.5% aluminum loading was set by the viscosity of the resulting nanofluid, where more aluminum powder resulted in a thick, gel-like mixture that could not be easily loaded into the propellant mount cavity with a pipette. Figure 14 shows the measured trends for

these mixtures and includes the previously described nitromethane baseline and mixture with 1% silica and 5% aluminum by weight.

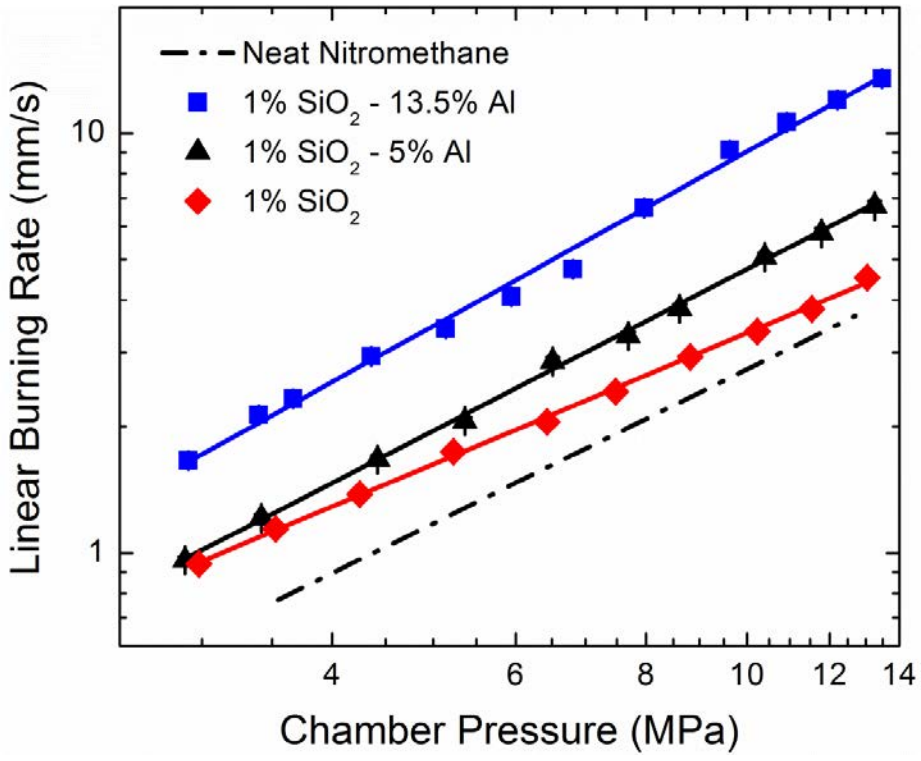

Fig. 14. Linear burning rates of nitromethane mixtures containing 1% fumed silica as functions of chamber pressure.

The added silica increased linear burning rates by 15% to 52% over those of neat nitromethane for all tested pressures and also increased empirical rate coefficients. The most important effect of the 1% silica additive was a marked decrease in the burning rate pressure exponent, matching similar observations from a previous study by Sabourin *et al.*, where the decreased pressure sensitivity was attributed to possible catalysis or gas flame stabilization over solid particles present in the combustion products [23].

Conversely, the added aluminum increased the pressure sensitivity of each mixture as a function of higher aluminum loading; this trend also matched behavior seen in the same study by Sabourin *et al*. [23]. The mixture of 1% silica and 5% aluminum increased linear burning rates by 61% to 77% over those of neat nitromethane, while the mixture of 1% silica and 13.5% aluminum increased linear burning rates by 172% to 249 % over those of the same baseline. The moderate 5% aluminum loading appeared to decrease the empirical coefficient of its mixture, yet the larger 13.5% loading reversed this trend with the increased coefficient of its respective mixture.

A separate study of nanostructured particle effects on nitromethane was completed by Sabourin *et al*. that attributed the burning rate enhancements from silica to increased thermal radiation output, the presence of catalytic processes, and an increase in the available surface area that all combined to increase the vaporization rate of the liquid nitromethane [34]. The combination of catalysis and a localized increase in heat capacity from particles near the burning surface was thought to reduce the reaction zone thickness, leading to a larger temperature gradient within the reaction zone and further increasing the rates of nitromethane vaporization and burning. For mixtures that contained aluminum nanoparticles, the energy feedback from their exothermic oxidation increased reaction zone temperatures and led to even greater rates of nitromethane vaporization and burning. The nano-scale aluminum likely also increased linear burning rates by providing a greater surface for nitromethane vaporization, but the much larger size and reduced specific surface area of the aluminum prevented this particular mechanism from becoming as prevalent as was seen with silica alone.

To better understand the effects of fumed silica on the combustion behavior of nitromethane and aluminum mixtures, a similar round of testing was completed with an increased silica loading of 3% by weight. This increased loading resulted in much greater mixture viscosities, severely limiting the amount of added aluminum to only 5%. Direct comparisons could still be made between these two mixture sets, because one of the previous mixtures had utilized the same 5% aluminum load. Figure 15 shows the measured trends for the two mixtures containing 3% silica by weight and compares them to a similar mixture tested by Sabourin *et al*. and the nitromethane baseline [23].

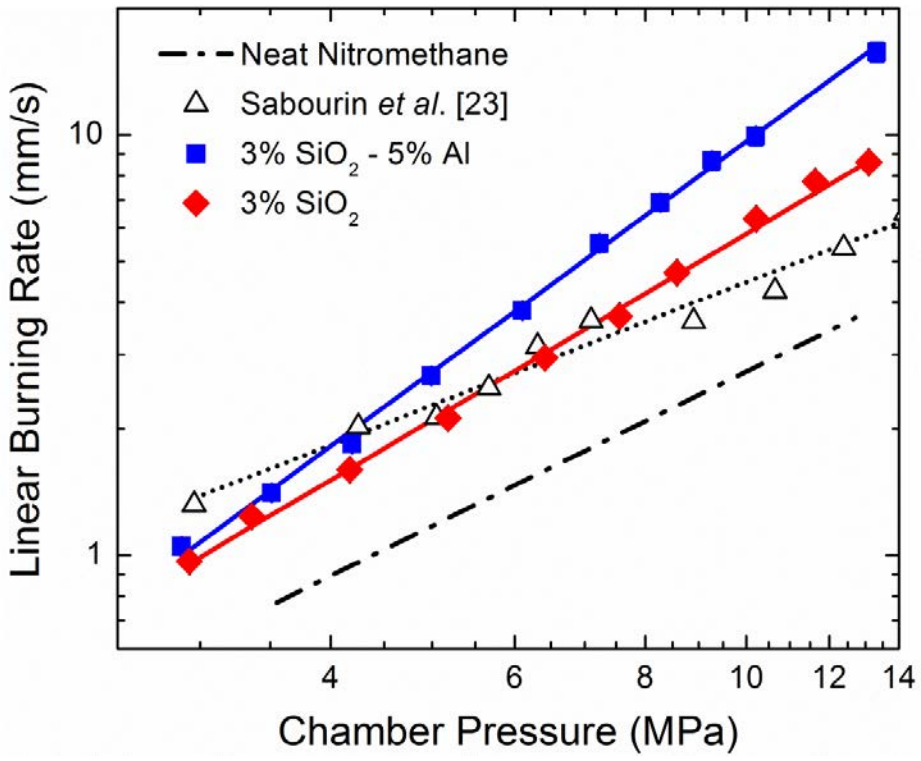

Fig. 15. Linear burning rates of nitromethane mixtures containing 3% fumed silica as functions of chamber pressure. Current data are compared to a similar mixture by Sabourin *et al*. [23].

As before, the added silica increased the linear burning rates and empirical coefficients over those of neat nitromethane for all tested pressures. However, the increased 3% silica loading resulted in burning rates that were 57% to 131% faster than the nitromethane baseline and actually increased the burning rate pressure exponent of its mixtures; this higher pressure sensitivity for greater silica loading was previously unobserved in other studies [22,23].

Interestingly, the presence of only 2% additional silica seen in Fig. 15 actually increased the burning rates and pressure sensitivity of its mixture more than the entire 5% of added aluminum seen in Fig. 14. Furthermore, the greater silica loading resulted in lower empirical coefficients than those seen for only 1% silica, affecting the mixture in much the same way as the aluminum presented in Fig. 14. These results imply that the addition of inert particles such as silica may not be a guaranteed way to decrease the pressure sensitivity of a given nanofluid; even the effects of an inert additive can be drastically changed by particle size and concentration. The mixture of 3% silica and 5% aluminum increased linear burning rates by 71% to 331% over those of the nitromethane baseline, and the added aluminum consistently decreased the empirical coefficient and increased the pressure exponent of its burning rate curve.

The similar mixture examined by Sabourin *et al*. in their previous study was comprised of nitromethane with 3% CAB-O-SIL TS-720 fumed silica and 4%, 80-nm aluminum by weight [23]. Their aluminum particles were comprised of 81% active aluminum by weight, and the reported 4% aluminum percentage was exclusive of any oxide coating. The 100-nm aluminum used in the current study was thought to contain a

similar amount of active aluminum because of its comparable size and shape, making the oxide-exclusive percentage of the current aluminum to be approximately 4% as well. Despite these similarities in additive materials and weight percentages, the mixture of silica and aluminum from the current study exhibited a much greater pressure sensitivity and faster burning rate than the previously studied mixture for all but the lowest tested chamber pressures. This disparity likely stemmed from the significant difference between the specific surface area of the currently used fumed silica powder, 200 m^2/g, and that of the silica used by Sabourin *et al*., 115 m^2/g [23].

While the addition of silica was shown to increase linear burning rates through catalysis and various heat transfer mechanisms, this improvement was balanced against a decrease in the energy density of any mixture containing the inert nanoparticles. For the particular silica used by Sabourin *et al*., the results of this trade-off were only favorable at weight percentages below 5% with a maximum in performance at approximately 1% loading [23]. The larger specific surface area of the silica used in the current study greatly enhanced the ability of a given weight percentage to increase linear burning rates through the aforementioned physical mechanisms. This larger silica surface area shifted the balance of the trade-off toward greater weight percentages, allowing the overall effect of silica addition to remain beneficial for greater loading and increasing the loading percentage where maximum performance occurred.

The nano-scale aluminum used in the current study was shown to consistently increase the pressure sensitivity of nitromethane-based mixtures at all added weight percentages, and a given weight percentage of aluminum had a greater effect on the

linear burning rates at higher pressures. For the case of aluminum added to a baseline mixture that also contained 1% silica by weight, relative increases in linear burning rates were measured for three levels of aluminum loading (0%, 5%, and 13.5% by weight). By estimating linear burning rates using the empirical trends later summarized in Section 4.5, the relative increases at each of the three specified aluminum loads can be calculated for any chamber pressure as shown in Fig. 16.

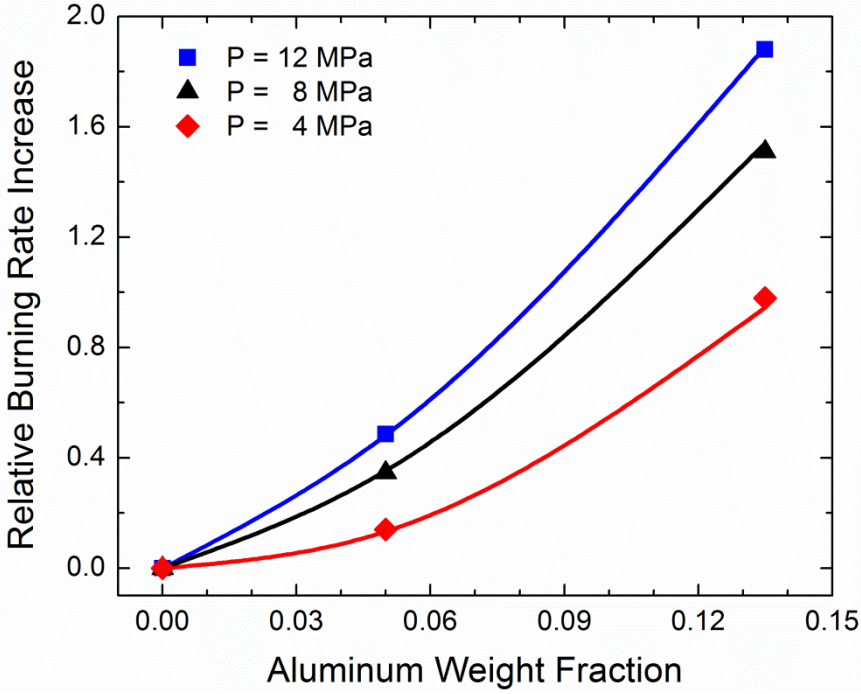

Fig. 16. Relative increases in burning rates as functions of aluminum loading. Percentage increase estimated for baseline mixture containing 99% nitromethane and 1% silica at chamber pressures of 4, 8, and 12 MPa. Lines represent predictions for each pressure using the correlation defined by Eq. (13).

The consistent, increasing effects of aluminum on mixture combustion allowed the relationship between the relative burning rate and aluminum load to be described by

similar quadratic equations for each specified chamber pressure. Upon further comparison, it was found that the second-order coefficient remained independent of the chamber pressure at an average value of approximately 51. On the other hand, the first-order coefficient did change with respect to the chamber pressure and became larger as the chamber pressure for each trial was increased. Furthermore, this relationship between the first-order coefficient and chamber pressure could be closely approximated by a logarithmic function over the range of tested pressures.

By combining a second-order coefficient that remained constant with a first-order coefficient that varied logarithmically as a function of pressure, the relative burning rate increase could be estimated at any reasonable aluminum load and chamber pressure. For the specific case of aluminum added to a mixture with 1% silica by weight, this estimate of the relative burning rate increase is represented by Eq. (13), with Y_{Al} defined as the weight fraction of aluminum and P defined as the chamber pressure in MPa.

$$\Delta r_b / r_b = 51.0\, {Y_{Al}}^2 + [6.35\, ln\, P - 8.69]\, Y_{Al} \tag{13}$$

Figure 16 shows the above correlation in comparison with the measured points; the maximum error of only 4% is reflected in the good agreement between Eq. (13) and the plotted data points. Of course, Eq. (13) is limited to the range of conditions of the present study and should not be extrapolated to conditions not covered herein, although it is useful for gauging the effect of pressure and aluminum loading on nitromethane mixtures.

While the effects of aluminum on the combustion behavior of nitromethane-based mixtures were found to be consistent at all weight percentages and more prevalent at higher pressures, the effects of fumed silica did not follow a similarly predictable trend. The pressure sensitivity of mixtures with silica shifted from decreasing to increasing between 1% and 3% addition by weight, while only the burning rate effects of the 3% silica loading were shown to be more prevalent at higher pressures. For the case of silica added to a baseline of neat nitromethane, relative increases in linear burning rates were measured for three levels of silica loading (0%, 1%, and 3% by weight). By again estimating linear burning rates using the empirical trends later summarized in Section 4.5, the relative increases at each of the three specified silica loadings can be calculated for any chamber pressure, as shown in Fig. 17.

The shift in pressure sensitivity and the circumstantial prevalence of burning rate effects at higher pressures inhibited the straightforward analysis of the fumed silica additive. Because of this changing dependency, it was unreasonable to create a single equation to accurately describe the relative burning rate effect of silica at any loading percentage and pressure without a greater number of tested loading percentages. However, a very rough approximation of the relationship between relative burning rates and the silica loading percentage can be taken for all pressures as a linear function of the loading percentage.

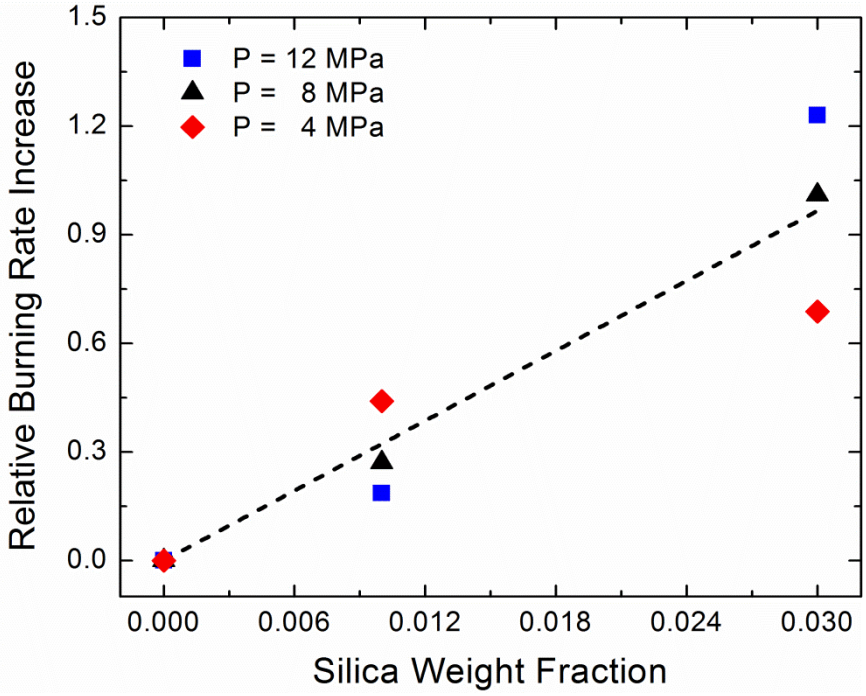

Fig. 17. Relative increases in burning rates as functions of silica loading. Percentage increase estimated for baseline of neat nitromethane at chamber pressures of 4, 8, and 12 MPa. The line represents the general correlation defined by Eq. (14).

This approximation is given in Eq. (14) as just a function of the silica loading and can be used to estimate the anticipated increase in linear burning rates for small silica loadings below 3% by weight, regardless of the chamber pressure.

$$\Delta r_b / r_b = 32.2\, Y_{SiO_2} \tag{14}$$

Y_{SiO2} represents the weight percentage of silica in the mixture, and Fig. 17 plots this correlation to compare with the range of experimental data. As mentioned above with regard to the correlation in Eq. (13), the correlation in Eq. (14) should also only be used for the range of silica loading conditions employed herein. It nonetheless reflects the roughly linear trend of increased burning rate with silica addition seen in the data.

4.5. Mixtures Containing Titania Catalyst

Recent collaborations between the authors' group and the University of Central Florida produced several studies that explored the use of nano-scale titania as a catalyst to alter the linear burning rates of solid propellants [35,36]. In a similar fashion, the present study investigated the effects of titania on the combustion behavior of nitromethane. The resulting behavior of those mixtures can be separated into two distinct groups: the segmented burning curves for those mixtures that contained titania without silica and the uniform burning curves for those mixtures that contained both titania and silica. Figure 18 shows the resulting trends for two mixtures that contained 1% titania by weight without any silica additive and compares them to the same currently established nitromethane baseline.

At tested chamber pressures below approximately 8 MPa, the effects of 1% titania on the pressure exponent and empirical coefficient were similar to those of the added 1% silica shown in Fig. 14. Increases in linear burning rates were also similar between the two separate additives, with improvements from titania ranging from 10% to 40% faster than the nitromethane baseline. However, this behavior abruptly shifted as the chamber pressure was increased above the 8-MPa threshold. At these elevated pressures, the mixture containing only 1% titania experienced a drastic increase in the burning rate pressure exponent and an equally dramatic decrease in the empirical coefficient of its burning curve. These changes resulted in linear burning rates that were over fourteen times faster than those of the nitromethane baseline at the upper limit of the tested chamber pressures. The shift in burning behavior above 8 MPa was also

accompanied by a greater inconsistency of measured burning rates at higher pressures, as evidenced by the elevated data scatter not found in any other tested mixture.

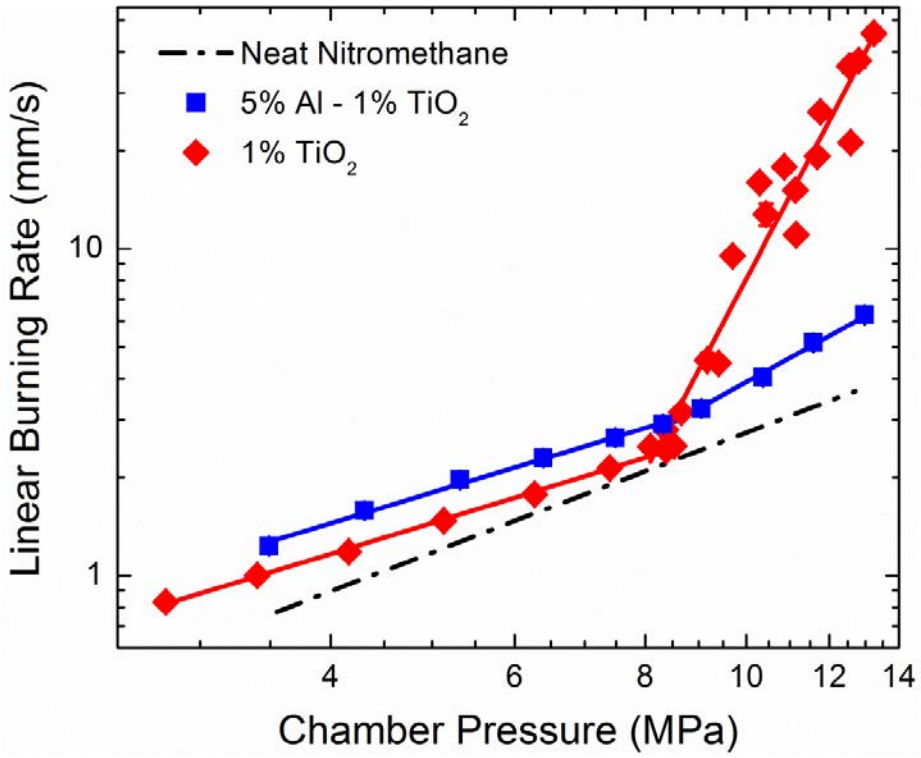

Fig. 18. Linear burning rates of nitromethane mixtures containing titania without silica as functions of chamber pressure.

While the addition of 5% aluminum by weight further increased the linear burning rates of mixtures at pressures below 8 MPa, this mixture was only 36% to 74% faster than neat nitromethane and still slower than the mixture containing 1% silica and 5% aluminum seen in Fig. 14. The lessened improvement of aluminum and titania below 8 MPa was expected, because the improvements caused by titania alone were similarly smaller than those caused by silica at lower chamber pressures. A similar shift in burning

behavior was seen for the mixture containing 1% titania and 5% aluminum at the same 8-MPa threshold, but the changes in the empirical coefficient and pressure exponent were much less dramatic than for titania alone and only resulted in burning rates that were elevated by 72% at the highest tested pressure.

Below 8 MPa, the burning rate enhancements from titania were thought to come from the very same mechanisms postulated for fumed silica. At chamber pressures below 8 MPa, the reduced effectiveness of titania as a burning rate enhancer when compared to silica can be explained by the smaller specific surface area and persistent agglomerates of the titania additive seen in Fig. 5. These two characteristics led to fewer sites for catalytic activity and nitromethane vaporization, limiting improvements in linear burning rates at lower pressures.

The abrupt changes in the burning rate curves of the two mixtures shown in Fig. 18 resembled the shift between burning regimes previously observed by Boyer, albeit at a lower pressure than the expected regime boundary at 15 MPa [5]. In a subsequent combustion model study, Boyer and Kuo attributed this change in burning behavior to the increased dissolution of gas-phase species in the liquid nitromethane at elevated chamber pressures [32]. It is possible that the titania additive encouraged the dissolution of these intermediate species into the liquid propellant, thereby driving the propellant mixture into the next burning regime at a lower chamber pressure than would be expected for nitromethane alone.

When comparing the emission spectra of propellant mixtures with titania to those without at wavelengths between 350 and 900 nm, no unique features were found at any

of the tested chamber pressures. The lack of any discernible emission bands at 530 nm ruled out the presence of titanium (II) oxide, a gaseous decomposition product of titania that would have indicated vaporization of the inert additive and provided another possible explanation for the slope breaks in both burning curves [37]. While the exact cause of the shift in combustion behavior was not revealed over the course of the current study, the dramatic and consistent elevation of burning rates above 8 MPa indicated a genuine effect of the titania additive that warrants further testing. The decreased severity of this burning shift caused by the added presence of aluminum further defied expectations, providing a similar opportunity for the additional study of nitromethane mixtures containing titania and other potential catalysts.

Despite the unanticipated changes in combustion behavior observed for the two mixtures in Fig. 18, the performance of mixtures containing both titania and silica reflected the uniform burning regime of the other mixtures shown in Figs. 14 and 15. The burning rate curves for mixtures containing both titania and silica are compared to the established nitromethane baseline in Fig. 19.

The combined presence of 1% titania and 1% silica by weight resulted in a pressure exponent and linear burning rates that were slightly less than for 1% silica alone, yielding mixture burning rates that were only 9% to 48% faster than those of the nitromethane baseline. This diminishing effect was also present in the addition of 1% titania to the mixture that included both 1% silica and 5% aluminum, resulting in burning rates that outpaced neat nitromethane by only 58%. The addition of aluminum had the same effect on the burning rate curve as was observed for mixtures in Figs. 14

and 15; the empirical coefficient was reduced, while the pressure exponent and linear burning rate was increased.

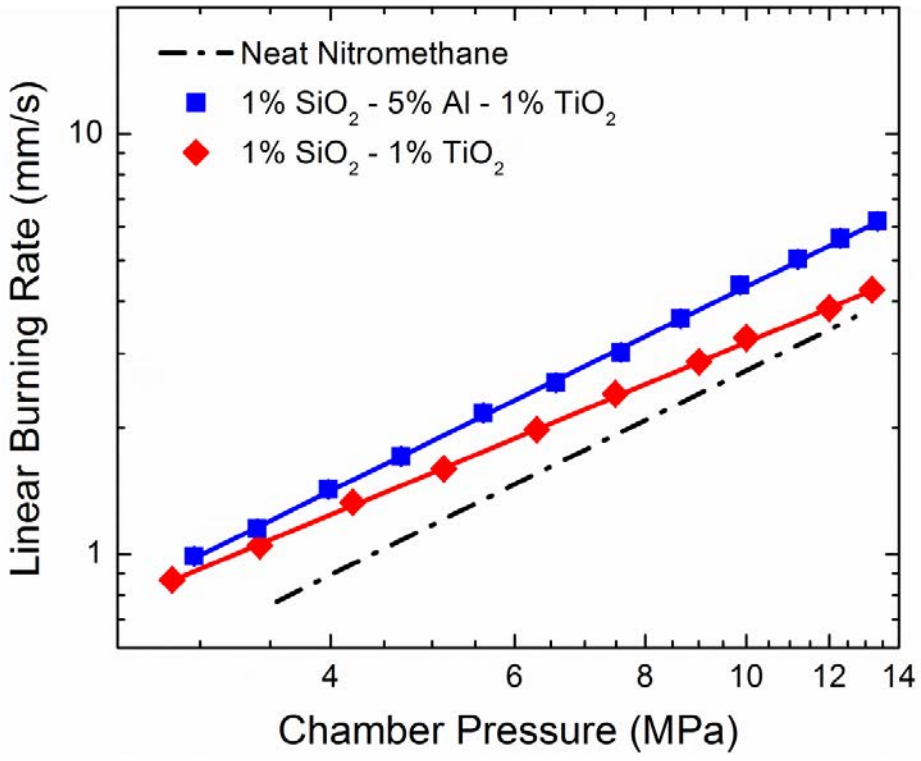

Fig. 19. Linear burning rates of nitromethane mixtures containing both titania and silica as functions of chamber pressure.

For the two mixtures that contained both 1% titania and 1% silica by weight, the increases in pressure exponents and linear burning rates fell between the improvements seen when separately using 1% silica or 1% titania. As previously discussed, the smaller specific surface area and visible agglomerates of the titania nanoparticles reduced the additive's ability for catalysis and nitromethane evaporation. Because of this diminished effectiveness, the accelerating effects of titania only outweighed the reduced energy

density of its mixtures for a smaller percentage of loaded particles than was already observed for the currently used silica. The loading percentage where maximum performance occurred was also thought to be smaller for the titania nanoparticles, mirroring the similar changes in particle loading and performance seen in Fig. 15 between the different silica additives used in the current study and previously by Sabourin *et al*. [23].

When adding both silica and titania to the same mixture, the doubled weight percentage of inert particles was not matched with an equivalent increase in catalysis and other accelerating effects to compensate for the decrease in mixture energy density. The ratio of positive-to-negative additive effects for the combined mixture of 1% titania and 1% silica was smaller than the ratio of effects for only 1% silica, justifying the slight decrease in burning rates observed with the addition of titania in Fig. 19. Determining the full range of beneficial weight percentages for the particular variety of silica and titania used by the authors, along with the exact weight percentages that provided maximum performance, did not fall within the scope of the current study. By including a wider variation of particle concentrations in future endeavors, the ability to optimize additive effects and propellant performance through the use of different loading percentages could be explored.

In all, ten unique nanofluids—consisting of nitromethane with known quantities of aluminum, silica, and titania—were evaluated in the strand burner system described herein. A definitive burning rate curve was created for neat nitromethane equal to

$$r_b[mm/s] = 0.165\ (P[MPa])^{1.22} \quad (3 < P \leq 14\ MPa) \tag{15}$$

that was used as a baseline to evaluate the performance of the other nitromethane-based mixtures. The final burning rate equation factors and statistical goodness-of-fit R^2 parameters of all ten configurations are compiled in Table 3 for review. The burner cavity material is specified for the two propellant formulations used to initially validate the author's system; the remaining mixtures were all tested using the quartz tube insert to promote burning at their inherent linear rates.

Table 3. Burning rate and R^2 parameters for tested monopropellant configurations.

Mixture	Empirical Coefficient (a)	Pressure Exponent (n)	R^2 Correlation
Neat Nitromethane (Steel)	0.289	1.06	0.985
Neat Nitromethane (Quartz)	0.165	1.22	0.999
1% SiO_2	0.305	1.04	0.999
1% SiO_2 - 5% Al (Steel)	0.267	1.25	0.999
1% SiO_2 - 5% Al (Quartz)	0.249	1.28	0.999
1% SiO_2 - 13.5% Al	0.377	1.38	0.995
3% SiO_2	0.197	1.47	0.998
3% SiO_2 - 5% Al	0.146	1.82	0.998
1% TiO_2 ($\leq$ 8 MPa)	0.301	0.976	0.998
1% TiO_2 ($\geq$ 8 MPa)	6.60×10^{-6}	6.09	0.946
5% Al - 1% TiO_2 ($\leq$ 8 MPa)	0.378	0.968	0.996
5% Al - 1% TiO_2 ($\geq$ 8 MPa)	6.64×10^{-2}	1.77	0.994
1% SiO_2 - 1% TiO_2	0.298	1.03	1.000
1% SiO_2 - 5% Al - 1% TiO_2	0.261	1.22	1.000

5. CONCLUSIONS*

5.1. Current Study

In this thesis, a robust technique was developed for measuring the linear burning rates of both liquid monopropellants and nanofluid mixtures without the need for direct visual observation. The burning rate equation of nitromethane defined using average chamber pressures and burning rates closely matched established results by other groups taken using instantaneous chamber pressures and optically-observed burning rates, proving the accuracy of the author's method.

The source of discrepancies between nitromethane burning rates measured in quartz and steel cavities was identified as a combination of heat transfer and catalytic effects, shaping the interpretation of future combustion measurements made with the author's system. Furthermore, the low scatter and consistent measurements taken for the aluminum and silica mixtures showed that the described technique can be utilized to test a wide variety of plain liquids and more-complex particle suspensions. By alleviating the need for direct observation of the traveling burning surface, the cost and complexity of the author's strand burner system was greatly reduced. This simplification allowed a single researcher to quickly test numerous samples without using large quantities of fuel or additives, all while collecting accurate and repeatable data.

---

*Part of this section is reprinted with permission from:
K.W. McCown III, A.R. Demko, E.L. Petersen, J. Propul. Power (2014) in press,
DOI: 10.2514/1.B35093, Copyright 2013 by the American Institute of Aeronautics and Astronautics;
K.W. McCown III, E.L. Petersen, Combust. Flame (2014) in press,
DOI: 10.1016/j.combustflame.2013.12.019, Copyright 2013 by the Combustion Institute.

The varied effects of commercially available nano-scale aluminum, fumed silica, and titania particles demonstrated the viability of using metal and metal-oxide additives to significantly alter the behavior of liquid monopropellants. The added aluminum particles consistently increased linear burning rates in all relevant mixtures, while pressure sensitivities were increased in all but one mixture: 1% titania and 5% aluminum by weight. Fumed silica nanoparticles consistently increased linear burning rates but were capable of either increasing or decreasing the pressure sensitivities of mixtures depending on the additive concentration. The opposing changes in the pressure sensitivity of nitromethane caused by differing percentages of silica were observed for the first time in the current study, implying that these particles can influence the temperature and pressure sensitivities of mixtures in radically different ways when present at different loading percentages

When comparing the two oxides used in the current study, fumed silica and titania, the smaller specific surface area of the titania powder reduced its effectiveness as a burning rate modifier under most conditions. However, the two mixtures containing 1% titania with or without 5% aluminum exhibited dramatic shifts in burning behavior at chamber pressures above 8 MPa, inviting further testing to identify the cause of these unexpected performance enhancements at certain conditions.

5.2. Other Studies in Progress

The techniques developed over the course of this thesis have already been applied to the formulation and evaluation of several EILs based on aqueous HAN. These

propellants contain various quantities of methanol and nanoparticle additives, fully exercising the capabilities of the author's system to measure the linear burning rates of complex, heterogeneous monopropellants. This testing continues to expand the range of viable hydrazine alternatives that can be evaluated at Texas A&M University, increasing the foothold of its researchers in the promising field of safer, environmentally friendly rocket propellants.

REFERENCES

[1] T. Edwards, J. Propul. Power 19 (6) (2003) 1089-1107.

[2] K. Anflo, T.A. Grönland, N. Wingborg, Development and Testing of ADN-Based Monopropellants in Small Rocket Engines, AIAA Paper No. 2000-3162, July, 2000.

[3] J.L. Sabourin, G.A. Risha, R.A. Yetter, S.F. Son, B.C. Tappan, Combust. Flame 154 (3) (2008) 587-600.

[4] A. Chowdhury, S.T. Thynell, Propell. Explos. Pyrot. 35 (6) (2010) 572-581.

[5] E. Boyer, Combustion Characteristics and Flame Structure of Nitromethane Liquid Monopropellant, PhD thesis, The Pennsylvania State University, University Park, PA, 2005.

[6] E.J. Wucherer, S. Christofferson, B. Reed, Assessment of High Performance HAN-Monopropellants, AIAA Paper No. 2000-3872, July, 2000.

[7] W.F. McBratney, J.A. Vanderhoff, High Pressure Windowed Chamber Burn Rate Determination of Liquid Propellant XM46, Report No. ARL-TR-442, U.S. Army Research Lab, Aberdeen Proving Ground, MD, 1994.

[8] W.F. Oberle, G.P. Wren, Burn Rates of LGP 1846 Conditioned Ambient, Hot, and Cold, Report No. BRL-TR-3287, U.S. Army Research Lab, Aberdeen Proving Ground, MD, 1991.

[9] Y.P. Chang, K.K. Kuo, J. Propul. Power 18 (5), (2002) 1076-1085.

[10] Y.P. Chang, J.K. Josten, B.Q. Zhang, K.K. Kuo, B.D. Reed, Combustion Characteristics of Energetic HAN/Methanol Based Monopropellants, AIAA Paper No. 2002-4032, July, 2002.

[11] D.T. Wickham, R. Cook, S. De Voss, J.R. Engel, J. Nabity, J. Russ. Laser Res. 27 (6) (2006) 552-561.

[12] G.A. Risha, S.F. Son, R.A. Yetter, V. Yang, B.C. Tappan, Proc. Combust. Inst. 31 (2) (2007) 2029-2036.

[13] T.K. Rice, J.B. Cole, Liquid Monopropellants Burning Rate of Nitromethane, Report No. NAVORD-2885, Naval Ordnance Lab, White Oak, MD, 1953.

[14] V.M. Raikova, Limit Conditions of Combustion and Detonation of Nitroesters and Mixtures on their Base, PhD thesis, Mendeleev Institute of Chemical Technology, Moscow, 1977.

[15] A. Alfano, J. Mills, G. Vaghjiani, Combust. Sci. Technol. 181 (6) (2009) 902-913.

[16] K.K. Kuo, Y.P. Chang, E. Boyer, Intrinsic Burning Behavior and Flame Structure Diagnostics of Liquid Propellants, Report No. 20001124 014, U.S. Army Research Office, Research Triangle Park, NC, 2000.

[17] M. Smiglak, W.M. Reichert, J.D. Holbrey, J.S. Wilkes, L. Sun, J.S. Thrasher, K. Kirichenko, S. Singh, A.R. Katritzky, R.D. Rogers, Chem. Commun. (Cambridge, U.K.) 24 (2006) 2554-2556.

[18] E. Boyer, D. Koch, K.K. Kuo, Y.C. Lu, Intrinsic Burning Rate and Temperature Sensitivity of Nitromethane, 34th JANNAF Combustion Subcommittee Meeting, Palm Beach, FL, 1997.

[19] S. Kelzenberg, N. Eisenreich, W. Eckl, V. Weiser, Propellants, Explos., Pyrotech. 24 (3) (1999) 189-194.

[20] E. Boyer, K.K. Kuo, High-pressure Combustion Behavior of Nitromethane, AIAA Paper No. 99-2358, June, 1999.

[21] G.P. Sutton, O. Biblarz, Rocket Propulsion Elements, 7th ed., John Wiley & Sons, New York, NY, 2001.

[22] V. Weiser, N. Eisenreich, S. Kelzenberg, Y. Plitzko, E. Roth, Influence of ALEX and Other Aluminum Particles on Burning Behavior Gelled Nitromethane Propellants, International Autumn Seminar on Propellants, Explosives, and Pyrotechnics (IASPEP 2005), Beijing, 2005.

[23] J.L. Sabourin, R.A. Yetter, B.W. Asay, J.M. Lloyd, V.E. Sanders, G.A. Risha, S.F. Son, Propellants, Explos., Pyrotech. 34 (5) (2009) 385-393.

[24] J.L. Sabourin, D.M. Dabbs, R.A. Yetter, F.L. Dryer, I.A. Aksay, ACS Nano 3 (12) (2009) 3945-3954.

[25] W.C. Warren, Experimental Techniques for the Study of Liquid Monopropellant Combustion, MS thesis, Texas A&M University, College Station, TX, 2012.

[26] S. Goroshin, D.L. Frost, J. Levine, A. Yoshinaka, F. Zhang, Propellants, Explos., Pyrotech. 31 (3) (2006) 169-181.

[27] E.L. Petersen, J. Arvanetes, A. LePage, R. Carro, A. Powell, Monitoring Strand Burner Combustion Products Using Emission Spectroscopy, AIAA Paper No. 2007-5767, July, 2007.

[28] S. Goroshin, J. Mamen, A. Higgins, T. Bazyn, N. Glumac, H. Krier, Proc. Combust. Inst. 31 (2) (2007) 2011-2019.

[29] U. Teipel, U. Förter-Barth, J. Propul. Power 21 (1) (2005) 40-43.

[30] H.M. Kindsvater, K.K. Kendall, K.H. Mueller, P.P. Datner, Research on Nitromethane, Report No. 493, Aerojet Engineering Corp., Azusa, CA, 1951.

[31] C.A. Frazier, Modeling Solid Propellant Strand Burner Experiments with Catalytic Nanoparticle Additives, PhD Dissertation, Texas A&M University, College Station, TX, 2011.

[32] E. Boyer, K.K. Kuo, Proc. Combust. Inst. 31 (2) (2007) 2045-2053.

[33] M.N. Özişik, Heat Conduction, John Wiley & Sons, New York, NY, 1980.

[34] J.L. Sabourin, R.A. Yetter, V.S. Parimi, J. Propul. Power 26 (5) (2010) 1006-1015.

[35] M.A. Stephens, E.L. Petersen, R. Carro, D.L. Reid, S. Seal, Propellants, Explos., Pyrotech. 35 (2) (2010) 143-152.

[36] D.L. Reid, K.R. Kreitz, M.A. Stephens, J.E.S. King, P. Nachimuthu, E.L. Petersen, S. Seal, J. Phys. Chem. C 115 (21) (2011) 10412-10418.

[37] A.B. Barrett, E.L. Petersen, Vaporization of Single- and Two-Component TiO_2 and SiO_2 Nanoparticles and Their Resulting Emission Spectra, Proceedings of the 2008 Technical Meeting of the Central States Section of the Combustion Institute, Tuscaloosa, AL, 2008.

Published Material Used with Permission

K.W. McCown III, A.R. Demko, E.L. Petersen, J. Propul. Power (2014) in press,

DOI: 10.2514/1.B35093.

K.W. McCown III, E.L. Petersen, Combust. Flame (2014) in press,

DOI: 10.1016/j.combustflame.2013.12.019.

APPENDIX A

A.1. Supplementary Equations for Analytical Models

The norm of the temperature equation used to describe the radial heat transfer model is a function of its associated eigenvalues and utilizes Bessel functions of the first kind (J_v). It is defined by its inverse in Eq. (A1),

$$1/N(\beta_i) = \pi^2 \beta_i^2 J_0^2(\beta_i r_1)/[2B_2 J_0^2(\beta_i r_1) - 2V_0^2] \tag{A1}$$

where B_2 and V_0 are abbreviated equations defined by Eq. (A2) and (A3),

$$B_2 = H^2 + \beta_i^2 \tag{A2}$$

$$V_0 = \beta_i J_1(\beta_i r_2) + H J_0(\beta_i r_2) \tag{A3}$$

and the modified convection coefficient for the outer burner tube surface (H) is defined by the convection coefficient of the fluid outside the burner tube (h) and the thermal conductivity of the tube material in Eq. (A4).

$$H = h/k \tag{A4}$$

The eigenfunction of the radial model equation is a function of its associated eigenvalues and radial position, and it includes Bessel functions of the first and second (Y_v) kind. It is defined by Eq. (A5),

$$R_0(\beta_i, r) = S_0 J_0(\beta_i r) - V_0 Y_0(\beta_i r) \tag{A5}$$

where S_0 is an abbreviated equation defined by Eq. (A6).

$$S_0 = \beta_i Y_1(\beta_i r_2) + H Y_0(\beta_i r_2) \tag{A6}$$

The eigenvalues of the radial model equation are equal to the positive roots of Eq. (A7),

$$0 = S_0 J_0(\beta_i r_1) - V_0 Y_0(\beta_i r_1) \tag{A7}$$

where the accuracy of the temperature profile is increased by calculating and implementing a greater number of eigenvalues. The initial temperature function of the radial model equation is a constant value related to the initial burner tube temperature (T_0) and propellant burning surface temperature and defined by Eq. (A8).

$$F = T_0 - T_s \tag{A8}$$

The norm of the temperature equation used to describe the axial heat transfer model is simply a function of the burner cavity length and is defined by its inverse in Eq. (A9).

$$1/N(\beta_i) = 2/L \tag{A9}$$

The eigenfunction of the axial model equation is a function of its associated eigenvalues and axial position, and it is defined by Eq. (A10).

$$X(\beta_i, x) = sin\,\beta_i x \tag{A10}$$

The eigenvalues of the axial model equation are equal to the positive roots of Eq. (A11),

$$0 = cos\,\beta_i L \tag{A11}$$

where the accuracy of the temperature profile is again increased by calculating and implementing a greater number of eigenvalues. The initial temperature function of the axial model equation is the same constant value that was used for the radial model equation shown in Eq. (A8), since both equations utilized the same initial burner tube and propellant burning surface temperatures.

A.2. Supplementary Equations for Numerical Approximations

For the radial heat transfer algorithm, the internal nodes between the constant temperature boundary at 535 K and the convective boundary to quiescent air are defined

by the temperatures at adjacent times and radii ($T_{r,t}$), material thermal diffusivity, time step (δt), radius step (δr), and adjacent radial positions. The explicit finite-difference form is shown in Eq. (A12).

$$T_{r,t+1} = T_{r,t} + \frac{\alpha \delta t}{r \delta r^2}\left[(r - \delta r/2\,)T_{r-1,t} - 2rT_{r,t} + (r + \delta r/2\,)T_{r+1,t}\right] \quad \text{(A12)}$$

The convective boundary nodes are defined by the temperatures at adjacent times and radii, material thermal diffusivity, time step, radius step, adjacent radial positions, fluid convection coefficient, material thermal conductivity, and fluid temperature (T_∞). The explicit finite-difference form is shown in Eq. (A13).

$$T_{r,t+1} = T_{r,t} + 2\frac{\alpha \delta t}{\delta r^2}\left[T_{r-1,t} - T_{r,t} - \delta r\left(\frac{r+\delta r/2}{r}\right)\left(\frac{h}{k}\right)\left(T_{r,t} - T_\infty\right)\right] \quad \text{(A13)}$$

For the axial heat transfer algorithm, the internal nodes between the constant temperature boundary at 535 K and the adiabatic boundary are defined by the temperatures at adjacent times and heights ($T_{x,t}$), material thermal diffusivity, time step, and height step (δx). The explicit finite-difference form is shown in Eq. (A14).

$$T_{x,t+1} = T_{x,t} + \frac{\alpha \delta t}{\delta x^2}\left[T_{x+1,t} - 2T_{x,t} + T_{x-1,t}\right] \quad \text{(A14)}$$

The adiabatic boundary nodes are defined by the temperatures at adjacent times and heights, material thermal diffusivity, time step, and height step. The explicit finite-difference form is shown in Eq. (A15).

$$T_{x,t+1} = T_{x,t} + 2\frac{\alpha \delta t}{\delta x^2}\left[T_{x+1,t} - T_{x,t}\right] \quad \text{(A15)}$$

The step sizes of the time and radius variables were chosen to ensure the stability of the meshes generated by the two explicit finite-difference algorithms. To simulate the perfect thermal contact boundary between the layers of quartz and steel, the respective

thermal diffusivities of the materials on either side of the boundary were used with the same internal node formulas given in Eq. (A12) and (A14).

APPENDIX B

The following tables contain the raw chamber pressures and linear burning rates for all propellant mixtures measured in the current thesis.

Table B1. Average chamber pressures and linear burning rates for neat nitromethane.

Chamber Pressure (MPa)	Linear Burning Rate (mm/s)
3.55	0.76
4.24	0.96
4.93	1.18
5.95	1.47
6.73	1.71
7.75	2.02
9.12	2.44
10.28	2.81
11.70	3.27
12.71	3.73

Table B2. Average chamber pressures and linear burning rates for 99% nitromethane and 1% silica by weight.

Chamber Pressure (MPa)	Linear Burning Rate (mm/s)
2.98	0.94
3.53	1.14
4.25	1.38
5.23	1.74
6.43	2.05
7.48	2.42
8.82	2.93
10.23	3.37
11.55	3.81
13.05	4.53

Table B3. Average chamber pressures and linear burning rates for 94% nitromethane, 1% silica, and 5% aluminum by weight.

Chamber Pressure (MPa)	Linear Burning Rate (mm/s)
2.89	0.96
3.42	1.21
4.42	1.67
5.36	2.06
6.51	2.86
7.69	3.29
8.62	3.82
10.40	5.07
11.79	5.78
13.26	6.71

Table B4. Average chamber pressures and linear burning rates for 85.5% nitromethane, 1% silica, and 13.5% aluminum by weight.

Chamber Pressure (MPa)	Linear Burning Rate (mm/s)
2.91	1.66
3.40	2.13
3.67	2.33
4.36	2.94
5.14	3.42
5.94	4.08
6.81	4.74
7.97	6.63
9.63	9.12
10.92	10.62
12.21	12.00
13.48	13.50

Table B5. Average chamber pressures and linear burning rates for 97% nitromethane and 3% silica by weight.

Chamber Pressure (MPa)	Linear Burning Rate (mm/s)
2.93	0.97
3.36	1.24
4.17	1.60
5.18	2.12
6.41	2.95
7.56	3.70
8.58	4.70
10.22	6.31
11.64	7.73
13.10	8.60

Table B6. Average chamber pressures and linear burning rates for 92% nitromethane, 3% silica, and 5% aluminum by weight.

Chamber Pressure (MPa)	Linear Burning Rate (mm/s)
2.88	1.05
3.51	1.41
4.19	1.84
4.99	2.67
6.10	3.82
7.23	5.51
8.27	6.90
9.27	8.67
10.21	9.92
13.33	15.73

Table B7. Average chamber pressures and linear burning rates for 99% nitromethane and 1% titania by weight.

Chamber Pressure (MPa)	Linear Burning Rate (mm/s)
2.78	0.83
3.40	1.00
4.16	1.18
5.13	1.47
6.27	1.77
7.40	2.13
8.09	2.48
8.37	2.79
8.38	2.41
8.53	2.49
8.66	3.16
9.17	4.56
9.40	4.46
9.70	9.51
10.29	15.97
10.44	12.76
10.87	17.79
11.14	15.12
11.16	11.05
11.69	19.19
11.77	26.25
12.54	36.19
12.58	21.15
12.81	37.71
13.24	45.66

Table B8. Average chamber pressures and linear burning rates for 94% nitromethane, 5% aluminum, and 1% titania by weight.

Chamber Pressure (MPa)	Linear Burning Rate (mm/s)
3.49	1.23
4.31	1.58
5.32	1.96
6.39	2.29
7.49	2.64
8.32	2.90
9.05	3.24
10.37	4.04
11.59	5.16
12.98	6.27

Table B9. Average chamber pressures and linear burning rates for 98% nitromethane, 1% silica, and 1% titania by weight.

Chamber Pressure (MPa)	Linear Burning Rate (mm/s)
2.82	0.87
3.42	1.05
4.20	1.33
5.13	1.60
6.30	1.98
7.49	2.41
9.01	2.87
10.00	3.27
12.00	3.85
13.19	4.26

Table B10. Average chamber pressures and linear burning rates for 93% nitromethane, 1% silica, 5% aluminum, and 1% titania by weight.

Chamber Pressure (MPa)	Linear Burning Rate (mm/s)
2.96	0.99
3.40	1.15
3.98	1.43
4.67	1.71
5.60	2.17
6.57	2.56
7.58	3.02
8.65	3.63
9.86	4.37
11.20	5.03
12.30	5.64
13.35	6.19